Available online at www.sciencedirect.com
SCIENCE DIRECT®
Journal of Computational Physics 197 (2004) 28–57
JOURNAL OF COMPUTATIONAL PHYSICS
www.elsevier.com/locate/jcp

Uncertainty propagation using Wiener–Haar expansions ☆

O.P. Le Maître [a,1], O.M. Knio [d,*], H.N. Najm [b], R.G. Ghanem [c]

[a] Centre d'Etudes de Mécanique d'Ile de France, Université d'Evry Val d'Essonne, 91020 Evry, France
[b] Combustion Research Facility, Sandia National Laboratories, Livermore, CA 94550, USA
[c] Department of Civil Engineering, The Johns Hopkins University, Baltimore, MD 21218, USA
[d] Department of Mechanical Engineering, The Johns Hopkins University, Baltimore, MD 21218, USA

Received 4 April 2003; received in revised form 23 November 2003; accepted 24 November 2003
Available online 4 February 2004

Abstract

An uncertainty quantification scheme is constructed based on generalized Polynomial Chaos (PC) representations. Two such representations are considered, based on the orthogonal projection of uncertain data and solution variables using either a Haar or a Legendre basis. Governing equations for the unknown coefficients in the resulting representations are derived using a Galerkin procedure and then integrated in order to determine the behavior of the stochastic process. The schemes are applied to a model problem involving a simplified dynamical system and to the classical problem of Rayleigh–Bénard instability. For situations involving random parameters close to a critical point, the computational implementations show that the Wiener–Haar (WHa) representation provides more robust predictions that those based on a Wiener–Legendre (WLe) decomposition. However, when the solution depends smoothly on the random data, the WLe scheme exhibits superior convergence. Suggestions regarding future extensions are finally drawn based on these experiences.

Keywords: Wavelets; Polynomial Chaos; Stochastic process; Uncertainty quantification

☆ This work was supported by the Laboratory Directed Research and Development Program at Sandia National Laboratories, funded by the US Department of Energy. Support was also provided by the Defense Advanced Research Projects Agency (DARPA) and Air Force Research Laboratory, Air Force Materiel Command, USAF, under agreement number F30602-00-2-0612. The US government is authorized to reproduce and distribute reprints for Governmental purposes notwithstanding any copyright annotation thereon. Computations were performed at the National Center for Supercomputer Applications.

* Corresponding author. Tel.: +1-410-516-7736; fax: +1-410-516-7254/7274.
E-mail addresses: olm@iup.univ-evry.fr (O.P. Le Maître), knio@jhu.edu (O.M. Knio), hnnajm@ca.sandia.gov (H.N. Najm), ghanem@jhu.edu (R.G. Ghanem).

[1] OLM was supported in part by CNRS, through affiliation with the Laboratoire d'Informatique pour la Mécanique et les Sciences de l'Ingénieur, Orsay, France.

0021-9991/$ - see front matter © 2004 Elsevier Inc. All rights reserved.
doi:10.1016/j.jcp.2003.11.033

1. Introduction

The development of uncertainty quantification (UQ) schemes has been the subject of much recent interest, arising in large part due to the the increasing availability of large parallel computing platforms, the concurrent evolution of advanced numerical methods and algorithms, and the the development of complex physical and computational models. Uncertainty quantification can be instrumental in the development of these models, e.g. for the purpose of validation or in support of decision making analysis. This paper is part of an effort that explores the application of PC representations [1–8] to develop UQ methods for thermo-fluid problems.

Polynomial Chaos based methods have been extensively used for UQ in engineering problems of solid and fluid mechanics (e.g. analysis of stochastic elastic structures [8,9], flow through porous media [10,11], incompressible and zero-Mach-number flows [12–14], thermal problems [15,16], as well as combustion and reacting flows [17–19]). One of the attractive features of the PC representation concerns the efficiency of the resulting schemes, which can yield accurate predictions of the uncertainty at a small fraction of the cost of a Monte-Carlo approach [13].

One of the drawbacks of spectral PC representations, however, concerns potential limitations in situations where complex solutions arise, or when the dependence of the solution on the random input data varies rapidly. This limitation has been well known based on experiences with Wiener–Hermite (WHe) representations. In particular, the analysis of Chorin [7] indicates that in complex problems involving shock formation or an energy cascade, the WHe representation may cease to be practical.

In this paper we address a similar but different difficulty, arising in the case a random parameter in the neighborhood of a critical point. We further restrict our attention to particular situations where the solutions remain smooth and well behaved, but which can change dramatically, or even discontinuously, according to specific values of the uncertain data. Such sensitivity of the solution with regard to the random data can be viewed as a parameter shock or bifurcation. For reasons similar to those analyzed in [7], one may expect that Wiener–Hermite or other spectral expansions to fail to adequately describe the steep (or discontinuous) dependence of the solution on the random data. This study explores the possibility of overcoming this difficulty by using a wavelet-based PC expansion. In doing so, the present approach combines concepts of generalized PC expansions, originally introduced in [20–22], and of using of piecewise functions in stochastic Galerkin methods [23]. In contrast to global basis functions, wavelet representations naturally lead to localized decompositions which suggest the possibility of a more robust behavior albeit at the expense of slower rate of convergence.

Being our first attempt in the use of wavelet-based PC expansions, we restrict our attention to the one of the simplest families of wavelets, namely the Haar basis. In Section 2, the Wiener–Haar expansion of solutions dependent on random data is introduced, and the salient features of the resulting PC representation are briefly outlined. In Section 3, we first address a simple model problem consisting of a dynamical system having two isolated, stable fixed points. Depending on specific realizations of the random initial conditions, the solution converges to one stable fixed point or the other. Numerical simulations indicate that the WHa scheme can effectively resolve the random process, but that a WLe expansion is unsuitable in this case. A more complex situation is considered in Section 4, based on a stochastic version of the Rayleigh–Bénard problem. Specifically, we consider two cases involving a random Rayleigh number, with the uncertainty range either containing the critical point or lying entirely above the critical value. In both cases, the behavior of WHa and WLe expansions is contrasted. Major findings and possible extensions are finally outlined in Section 5.

2. The Wiener–Haar expansion

In this section, we construct a WHa representation of a stochastic process. We start in Section 2.1 with the decomposition of a one-dimensional probability space using Haar's wavelets, and construct in Section

2.2 the associated orthonormal decomposition of a random process. The construction is then generalized to the multi-dimensional case in Section 2.3. Solution methods are given in Section 2.4, together with a brief discussion of similarities and differences with spectral PC constructions [12,13].

2.1. Preliminaries

Let θ be a random variable with given statistics. We denote by $\mathrm{p}(x)$ the probability that $\theta < x$, and assume that $\mathrm{p}(x)$ is a continuous strictly increasing function of x defined on a real interval (a,b), such that $-\infty \leqslant a < b \leqslant \infty$, $\mathrm{p}(a) \equiv 0$ and $\mathrm{p}(b) \equiv 1$. Although extension to the infinite case is possible, we shall exclusively deal with the situation where a and b are finite. Using $\mathrm{p}(x)$, the probability density function of x on (a,b) is given by

$$\begin{aligned} &\mathrm{pdf}(x) \equiv \frac{\mathrm{dp}(x)}{\mathrm{d}x} > 0 \quad \forall x \in (a,b), \\ &\mathrm{pdf}(x) \equiv 0 \quad \forall x \notin (a,b). \end{aligned}$$

Based on the assumed properties of $\mathrm{p}(x)$, it follows that for all $y \in [0,1]$ there is a unique $x \in [a,b]$ such that $\mathrm{p}(x) = y$. Consequently, we define the one-to-one mapping

$$y \in [0,1] \to x \equiv \mathrm{p}^{-1}(y) \in [a,b]. \tag{1}$$

2.1.1. Haar scaling functions

The scaling function of the Haar system, denoted by $\phi^{\mathrm{w}}(y)$, is given by [24–27]

$$\phi^{\mathrm{w}}(y) = \mathbf{I}_{[0,1)}(y) = \begin{cases} 1, & 0 \leqslant y < 1, \\ 0, & \text{otherwise.} \end{cases} \tag{2}$$

Introducing the scaling factor j and the sliding factor k, we denote by

$$\phi^{\mathrm{w}}_{j,k}(y) = 2^{j/2}\phi^{\mathrm{w}}(2^j y - k), \tag{3}$$

the scaled Haar functions. Now, let $\{V_j\}_{j=0}^{\infty}$ be the sequence of function spaces defined by $V_j = \mathrm{span}\{\phi^{\mathrm{w}}_{j,k},\ k \in [0, 2^j - 1]\}$, and denote by $P^j f$ the projection of f onto the space V_j; we thus have

$$P^j f = \sum_{k=0}^{2^j-1} f_{j,k}\phi^{\mathrm{w}}_{j,k}(y), \tag{4}$$

where the coefficients are given by

$$f_{j,k} = \int_0^1 f(y)\phi^{\mathrm{w}}_{j,k}(y)\,\mathrm{d}y. \tag{5}$$

2.1.2. Haar wavelets

The detail function $g^{j-1} \in V_j$ is defined as the difference between two successive resolution levels, namely

$$g^{j-1} = P^j f - P^{j-1} f. \tag{6}$$

To obtain an expression of the detail function, we introduce the Haar function

$$\psi^{\mathrm{w}}(y) \equiv \frac{1}{\sqrt{2}}\phi^{\mathrm{w}}_{1,0}(y) - \frac{1}{\sqrt{2}}\phi^{\mathrm{w}}_{1,1}(y) = \begin{cases} 1, & 0 \leqslant y < \frac{1}{2}, \\ -1, & \frac{1}{2} \leqslant y < 1, \\ 0, & \text{otherwise.} \end{cases} \tag{7}$$

The Haar function is the *mother wavelet* that generates the wavelet family

$$\psi^{\mathrm{w}}_{j,k}(y) = 2^{j/2}\psi^{\mathrm{w}}(2^j y - k), \quad j = 0, 1, \ldots, \text{ and } k = 0, \ldots, 2^j - 1. \tag{8}$$

From this definition we have

$$\int_0^1 \psi^{\mathrm{w}}_{j,k}(y)\,\mathrm{d}y = 0 \quad \text{and} \quad \int_0^1 \psi^{\mathrm{w}}_{j,k}\psi^{\mathrm{w}}_{l,m}\,\mathrm{d}y = \delta_{jl}\delta_{km}. \tag{9}$$

Consequently, the set $\{\psi^{\mathrm{w}}_{j,k}; j = 0, 1, \ldots, \infty;\ k = 1, \ldots, 2^j - 1\}$ is an orthonormal system, and any function $f \in L^2([0,1])$ can be arbitrarily well approximated by the sum of its mean and a finite linear combination of the $\psi^{\mathrm{w}}_{j,k}(y)$.

In terms of wavelets, the detail function can be expressed as

$$g^{j-1}(y) = \sum_{k=0}^{2^j-1} d_{j,k}\psi^{\mathrm{w}}_{j-1,k}(y), \tag{10}$$

while $P^j f$ is given by

$$P^j f = P^0 f + \sum_{l=0}^{j-1}\sum_{k=0}^{2^l-1} d_{l,k}\psi^{\mathrm{w}}_{l,k}(y). \tag{11}$$

2.2. Wavelet approximation of a 1D random process

We now seek a wavelet representation of a second-order random process $X(\xi(\theta))$, where ξ is a random variable satisfying the assumptions of the previous section.

The notation $\xi(\theta)$ is used to denote the stochastic nature of ξ. Specifically, we consider an expansion of the form

$$X(\xi(\theta)) = X_0 + \sum_{j=0}^{\infty}\sum_{k=0}^{2^j-1} X^{\mathrm{w}}_{j,k}\mathbf{W}_{j,k}(\xi(\theta)), \tag{12}$$

where $X^{\mathrm{w}}_{j,k}$ are the coefficients of the wavelet approximation of $X(\xi)$,

$$\mathbf{W}_{j,k}(\xi \in [a,b]) \equiv \psi^{\mathrm{w}}_{j,k}(\mathrm{p}(\xi)), \tag{13}$$

and the equality is interpreted in mean-square sense. Eq. (12) can be rewritten as

$$X(\xi(\theta) \in [a,b]) = X_0 + \sum_{j=0}^{\infty}\sum_{k=0}^{2^j-1} X^{\mathrm{w}}_{j,k}\psi^{\mathrm{w}}_{j,k}(\mathrm{p}(\xi)), \tag{14}$$

where $X_0 \equiv P^0 X(\xi)$. Moreover, the ortho-normality of the Haar wavelets ensures that

$$\int_{[a,b]} \mathbf{W}_{j,k}(\xi)\mathbf{W}_{l,m}(\xi)\mathrm{pdf}(\xi)\,\mathrm{d}\xi = \int_0^1 \psi^{\mathrm{w}}_{j,k}(y)\psi^{\mathrm{w}}_{l,m}(y)\,\mathrm{d}y \equiv \delta_{j,l}\delta_{k,m}. \tag{15}$$

This shows that the set of wavelets $\{\mathrm{W}_{j,k}, j = 0,\ldots,\infty;\ k = 0,\ldots,2^j - 1\}$ forms an orthonormal system with respect to the inner product

$$\langle f, g\rangle \equiv \int_{[a,b]} f(\xi)g(\xi)\mathrm{pdf}(\xi)\,\mathrm{d}\xi$$

and that $\langle f\rangle$ coincides with the mean or expectation. The wavelet set $\{\mathrm{W}_{j,k}, j = 0,\ldots,\infty;\ k = 0,\ldots,2^j - 1\}$ in fact forms a basis of the space of second-order processes, $\{X : \langle X, X\rangle < \infty\}$ [25,24].

Let us denote by ∇ the set of index integers λ concatenating the scale index j and the space index k: $\nabla \equiv \{\lambda : \lambda = 2^j + k;\ j = 0,\ldots,\infty;\ k = 0,\ldots,2^j - 1\}$. The resolution level will be denoted by $|\lambda|$. Using these conventions, the one-dimensional wavelet expansion of $X(\theta)$ can be expressed as

$$X(\xi(\theta) \in [a,b]) = X_0 + \sum_{\lambda\in\nabla} X_\lambda \mathrm{W}_\lambda(\xi(\theta)). \tag{16}$$

Moreover,

$$X_0 \equiv \int_0^1 X(\mathrm{p}^{-1}(y))\phi^{\mathrm{w}}_{0,0}(y)\,\mathrm{d}y = \int_{[a,b]} X(\xi)\mathrm{pdf}(\xi)\,\mathrm{d}\xi = \langle X(\xi)\rangle \tag{17}$$

is the expected value of the process. Consequently, setting $\mathrm{W}_0 \equiv 1$, and denoting ∇_0 the extension of ∇ to include the index 0, the 1D wavelet expansion becomes

$$X(\xi(\theta) \in [a,b]) = \sum_{\lambda\in\nabla_0} X_\lambda \mathrm{W}_\lambda(\xi(\theta)), \tag{18}$$

where

$$X_\lambda \equiv \int_0^1 X(\mathrm{p}^{-1}(y))\psi^{\mathrm{w}}_\lambda(y)\,\mathrm{d}y = \int_{[a,b]} X(\xi)\mathrm{W}_\lambda(\xi)\mathrm{pdf}(\xi)\,\mathrm{d}\xi = \langle X(\xi)\mathrm{W}_\lambda(\xi)\rangle. \tag{19}$$

The expansion in Eq. (18) is the wavelet analogue of the generalized PC expansion used in stochastic spectral methods.

2.3. Multi-dimensional process

In this section, we extend the WHa expansion to the multi-dimensional case, and focus for simplicity on a vector ξ of independent random components $\{\xi_1(\theta),\ldots,\xi_N(\theta)\}$ obeying

$$\langle\xi_i\rangle = 0, \quad i = 1,\ldots,N, \qquad \text{and} \qquad \langle\xi_i\xi_j\rangle = \langle\xi_i^2\rangle\delta_{ij}, \quad 1 \leqslant i,j \leqslant N.$$

We now consider the multi-dimensional index $\boldsymbol{\lambda} = (\lambda_1, \lambda_2, \ldots, \lambda_N)$, and define the sequence

$$\mathscr{W}_n \equiv \left\{ \prod_{k=1}^N \mathrm{W}_{\lambda_k}(\xi_k) : \sum_{k=1}^N |\lambda_k| = n \right\}$$

to be the set of multi-dimensional wavelets having resolution n. The multi-dimensional wavelet expansion of $X(\xi(\theta))$ can now be formally written as [1,8]

$$X(\xi_1(\theta),\ldots,\xi_N(\theta)) = X_0\mathscr{W}_0 + \sum_{i_1=1}^{N} c_{i_1}\Gamma_1(\xi_{i_1}(\theta)) + \sum_{i_1=1}^{\mathbf{N}}\sum_{i_2=1}^{i_1} c_{i_1 i_2}\Gamma_2(\xi_{i_1}(\theta),\xi_{i_2}(\theta)) + \sum_{i_1=1}^{N}\sum_{i_2=1}^{i_1}\sum_{i_3=1}^{i_2} c_{i_1 i_2 i_3}\Gamma_3(\xi_{i_1}(\theta),\xi_{i_2}(\theta)\xi_{i_3}(\theta)) + \cdots, \tag{20}$$

where $\Gamma_0(\xi)\equiv 1$, and $\Gamma_k \in \mathscr{W}_k$ denotes a multi-dimensional wavelet of resolution k. In practice, the wavelet expansion must be truncated, and different strategies may be used for this purpose. The most intuitive approach is to retain wavelets of resolution n, i.e. we retain vectors $\boldsymbol{\lambda}$ such that $\sum_{k=1}^{N}|\lambda_k|\leqslant n$. In this case, the multi-dimensional resolution level n plays a similar role as the order in Wiener–Hermite expansions [1,8]. Another possibility is to use the "spherical truncation", e.g. by retaining vectors $\boldsymbol{\lambda}$ satisfying $\left(\sum_{k=1}^{N}|\lambda_k|^2\right)^{1/2}\leqslant n$.

Regardless of the truncation strategy, the truncated expansion may be conveniently rewritten as a single-index summation, according to

$$X(\xi)\approx\sum_{k=0}^{N_w} X_k^{\mathrm{w}}\mathscr{H}a_k(\xi(\theta)), \tag{21}$$

where N_w+1 is the dimension of the truncated basis, $\{\mathscr{H}a_k, k=0,\ldots,N_w\}$.

2.4. Comparison with spectral expansions

Similar to the WHe [1,8] and other spectral representations [20], the wavelet expansion (Eq. (21)) is an orthonormal approximation of the stochastic process. This property may be immediately exploited to extract the process expectation

$$\langle X\rangle = X_0^{\mathrm{w}},$$

and its variance

$$\sigma^2(X) = \sum_{k=1}^{N_w}\left(X_k^{\mathrm{w}}\right)^2.$$

Despite the formal similarities of the corresponding expansions, fundamental differences between wavelet and spectral representations should be noted. In the latter case, global orthogonal polynomials are specifically selected so that, when appropriate smoothness conditions are satisfied, an "infinite-order" convergence rate results. Such convergence rate is not expected for the WHa expansion, in which the basis functions are localized. Specifically, the WHa expansion derived above can be viewed as an "orthogonal sampling" or a local decomposition of the solution into piecewise constant processes. One may expect that in situations where the response of the system shows a localized sharp variation or a discontinuous change, the wavelet decomposition may be more efficient than a spectral expansion, whose convergence could dramatically deteriorate due to Gibbs-type phenomena. Another distinctive feature of the WHa expansion concerns products of piecewise constant processes. For instance, the product xy of two elements x and y of V_j also belongs to the same space. In contrast, the product of two polynomials of degree less than or equal to n does not necessarily belong to the space of polynomials having degree less than or equal to n. Thus, one may also expect that for problems exhibiting steep dependence on the random data the WHa scheme is less susceptible to aliasing errors than a spectral scheme. Below, we address these questions by considering situations involving both smooth and discontinuous dependence on the random data, and contrast the behavior of WHa and WLe expansions.

3. Model problem

We first apply the WHa decomposition to a simple model problem that involves a discontinuous dependence of the process on the random data. This provides a stringent test of the representation, as one expects that a global spectral expansion would exhibit severe difficulties in capturing the behavior of the stochastic process. To this end, results obtained using the WHa expansion are contrasted with predictions based on a WLe representation.

3.1. Problem statement

Consider the following deterministic differential equation:

$$\frac{\mathrm{d}^2x}{\mathrm{d}t^2} + f\frac{\mathrm{d}x}{\mathrm{d}t} = -\frac{\mathrm{d}h}{\mathrm{d}x}, \tag{22}$$

with parameters $f > 0$ and $\mathrm{d}h/\mathrm{d}x$. The problem requires two initial conditions: $x(t=0) = x_0$ and $v(t=0) \equiv \mathrm{d}x/\mathrm{d}t(t=0) = v_0$. The system can be interpreted as the governing equation for a particle moving under the influence of a potential field and of a friction force. In the computations below, we set $h(x) = (35/8)x^4 - (15/4)x^2$ so that the differential equation has two stable fixed points ($x = \pm\sqrt{15/35}$), and an unstable fixed point at $x = 0$. The potential field $h(x)$ and the function $\mathrm{d}h/\mathrm{d}x$ are plotted in Fig. 1.

A stochastic variant of the above system is constructed by considering an uncertain initial position x_0. On the other hand, the particle is always released with a vanishing velocity. In the computations, we assume that the initial position is uniformly distributed over the interval $[x_1, x_2]$, i.e. $\mathrm{pdf}(x_0 \in [x_1, x_2]) = 1/|x_2 - x_1|$ and $\int_{x_1}^{x_2} \mathrm{pdf}(x)\,\mathrm{d}x = 1$. The stochastic initial conditions can be expressed as

$$X(t=0,\xi) = X_0 + \Delta X\xi, \quad \left.\frac{\mathrm{d}X}{\mathrm{d}t}\right|_{t=0} = 0,$$

where $X(t,\xi)$ denotes the response of the stochastic system, $X_0 \equiv (x_1 + x_2)/2$, $\Delta X = |x_1 - x_2|/2$, and ξ is uniformly distributed over $[-1,1]$ with $\mathrm{pdf}(\xi) = 1/2$. Thus, the stochastic system can be formulated as

$$\frac{\mathrm{d}^2X}{\mathrm{d}t^2} + f\frac{\mathrm{d}X}{\mathrm{d}t} = -\frac{35}{2}X^3 + \frac{15}{2}X, \tag{23}$$

$$X(t=0,\xi) = X_0 + \Delta X\xi, \tag{24}$$

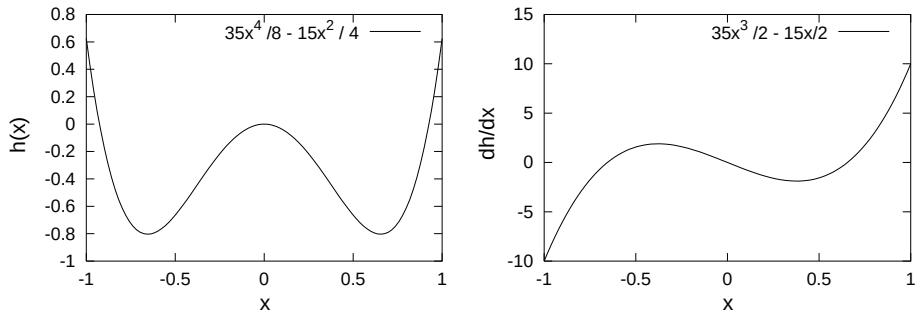

Fig. 1. Profiles of $h(x)$ and of $\mathrm{d}h/\mathrm{d}x$ for the model problem of Section 3.

$$\left.\frac{\mathrm{d}X}{\mathrm{d}t}\right|_{t=0} = 0. \tag{25}$$

3.1.1. Solution method

In this section, we outline the method used to integrate the stochastic formulation based on the WHa representation. The solution method for the WLe representation is similar and is consequently omitted.

The truncated WHa expansion of the solution process is expressed as

$$X(t,\xi(\theta)) \approx \tilde{X}(t,\xi) = \sum_{k=0}^{N_w} X_k^{\mathrm{w}}(t)\mathscr{H}a_k(\xi).$$

Governing equations for the wavelet coefficients X_k^{w} are derived in two steps. The truncated wavelet expansion is first inserted into Eq. (23), and projections onto the wavelet basis are then performed. The latter step is implemented by multiplying the expanded system by $\mathscr{H}a_l$ and then forming the expectation. This leads to a system of N_w+1 coupled ODEs for the coefficients

$$\frac{\mathrm{d}^2X_l^{\mathrm{w}}}{\mathrm{d}t^2} + f\frac{\mathrm{d}X_l^{\mathrm{w}}}{\mathrm{d}t} = -\frac{35}{2}\left\langle \tilde{X}^3\mathscr{H}a_l\right\rangle + \frac{15}{2}X_l^{\mathrm{w}} \tag{26}$$

for $l=0,\ldots,N_w$. A similar Galerkin approach is used to derive initial conditions for the individual modes; we get

$$X_0^{\mathrm{w}}(t=0) = X_0, \quad X_l^{\mathrm{w}}(t=0) = \Delta X\langle \xi\mathscr{H}a_l\rangle \quad \text{for } l=1,\ldots,N_w, \tag{27}$$

$$\left.\frac{\mathrm{d}X_l^{\mathrm{w}}}{\mathrm{d}t}\right|_{t=0} = 0 \quad \text{for } l=0,\ldots,N_w. \tag{28}$$

Eq. (26) can be easily integrated once the the cubic term, $\langle\tilde{X}^3\mathscr{H}a_l\rangle$, is determined. Two approaches are considered here, based on (i) a Galerkin approach, and (ii) a pseudo-spectral approximation. In order to outline these approaches, we first introduce the "multiplication tensor",

$$C_{ijk} \equiv \left\langle \mathscr{H}a_i\mathscr{H}a_j\mathscr{H}a_k\right\rangle$$

and "the triple product tensor",

$$T_{ijkl} \equiv \left\langle \mathscr{H}a_i\mathscr{H}a_j\mathscr{H}a_k\mathscr{H}a_l\right\rangle.$$

One can readily [8,12,13] show that the Galerkin approximation of quadratic term X^2 is given by

$$(X^2)_k^{\mathrm{w}} \equiv \left\langle \tilde{X}^2\mathscr{H}a_k\right\rangle = \sum_{i=0}^{N_w}\sum_{j=0}^{N_w} C_{ijk}X_i^{\mathrm{w}}X_j^{\mathrm{w}}.$$

In the Galerkin approach, the cubic term is obtained through convolution involving the triple tensor, specifically using the following triple sum:

$$(X^2)_l^{\mathrm{w}} \equiv \left\langle \tilde{X}^3\mathscr{H}a_l\right\rangle = \sum_{i=0}^{N_w}\sum_{j=0}^{N_w}\sum_{k=0}^{N_w} T_{ijkl}X_i^{\mathrm{w}}X_j^{\mathrm{w}}X_k^{\mathrm{w}}.$$

On the other hand, for the pseudo-spectral approach, the cubic term is approximated through repeated application of the binary multiplication operator, according to

$$(X^3)_k^{\mathrm{w}} \equiv \left\langle (X^3)\mathscr{H} a_k \right\rangle = \left\langle (X)(X^2)\mathscr{H} a_k \right\rangle \simeq \sum_{i=0}^{N_w}\sum_{j=0}^{N_w} C_{ijk} X_i^{\mathrm{w}} (X^2)_j^{\mathrm{w}}.$$

The tensor C_{ijk} (and when present T_{ijkl}) is evaluated in a pre-processing step and then stored for later use in the simulations. This evaluation, as well as several useful transformations, such as products and inverse transformations, are implemented using a software library of routines which we call the UQ toolkit. This library was initially developed for Wiener–Hermite representations [18,28], but was extended to include the presently considered expansions. Note that, similar to the Hermite and Legendre systems, the multiplication tensor in the Haar system is sparse and can be evaluated exactly. Also note that in the case of the WHa expansion, the pseudo-spectral approach coincides with the Galerkin estimate. This is the case because, as previously noted, the product of elements of V_j also belongs to V_j. For the WLe and other polynomial representations, on the other hand, repeated binary products introduce aliasing errors due to truncation at the intermediate stages.

The time integration of Eq. (26) is performed using a fourth-order Runge–Kutta scheme. In all computations described in this section, a small value of the time step was used, $\Delta t = 0.001$. This value was selected following a straightforward analysis in which the time step was systematically reduced until it had negligible impact on the predictions.

Below, we compare solutions obtained using the WHa expansion, truncated to a given resolution level N_{r}, with results obtained using both Galerkin and pseudo-spectral WLe expansions, truncated to order N_{o}. Since we are dealing with a single stochastic dimension, the total number of basis functions in the WHa expansion is equal to $2^{N_{\mathrm{r}}}$; in the case of WLe, it is equal to $N_{\mathrm{o}} + 1$.

3.2. Results

3.2.1. WLe scheme

The WLe scheme is applied to the model problem above, with stochastic initial conditions specified by $X_0 = 0.05$ and $\Delta X = 0.2$. A relatively large value of the friction coefficient is selected, $f = 2$, so that a steady solution is achieved in a short time. For the present conditions, the analytical prediction of the steady state is given by

$$\begin{cases} X(t\to\infty,\xi) = -\sqrt{15/35}, & \xi < -0.25, \\ X(t\to\infty,\xi) = \sqrt{15/35}, & \xi > -0.25, \end{cases}.$$

which results in the following statistical moments, $\langle X(t\to\infty,\theta)\rangle = 0.163663$ and $\sigma(t\to\infty,\theta) >= 0.633865691$.

Figs. 2 and 3, respectively, depict the pseudo-spectral and Galerkin WLe solutions for different expansion orders. Plotted are the short-time evolution of $X(t,\xi)$, the solution at $t = 10$, and the corresponding "steady-state" pdf of X. The results indicate that, regardless of the order of the expansion, the WLe scheme does not provide an adequate representation of the behavior of the system. Specifically, unphysical oscillations in the distribution of $X(\xi)$ are observed, which are more pronounced in the pseudo-spectral computations than in the Galerkin results. These oscillations are still present in the "large time" steady solution, as shown in Fig. 4. Around the equilibrium points $X = \pm\sqrt{15/35}$, the amplitude of the wiggles decreases slightly as N_{o} increases, but their frequency increases. The manifestation of these wiggles is reminiscent of the Gibbs phenomenon which occurs in spectral decompositions of discontinuous signals. The impact of this phenomenon can also be appreciated in the predicted steady-state pdf of X, shown in the right column of Figs. 2 and 3. For the present stochastic problem, the analytical pdf consists of two Dirac masses of unequal strength, located at the stable equilibrium points $X = \pm\sqrt{15/35}$. The WLe predictions differ significantly from the analytical prediction; around the equilibrium points, they exhibit a broad spectrum

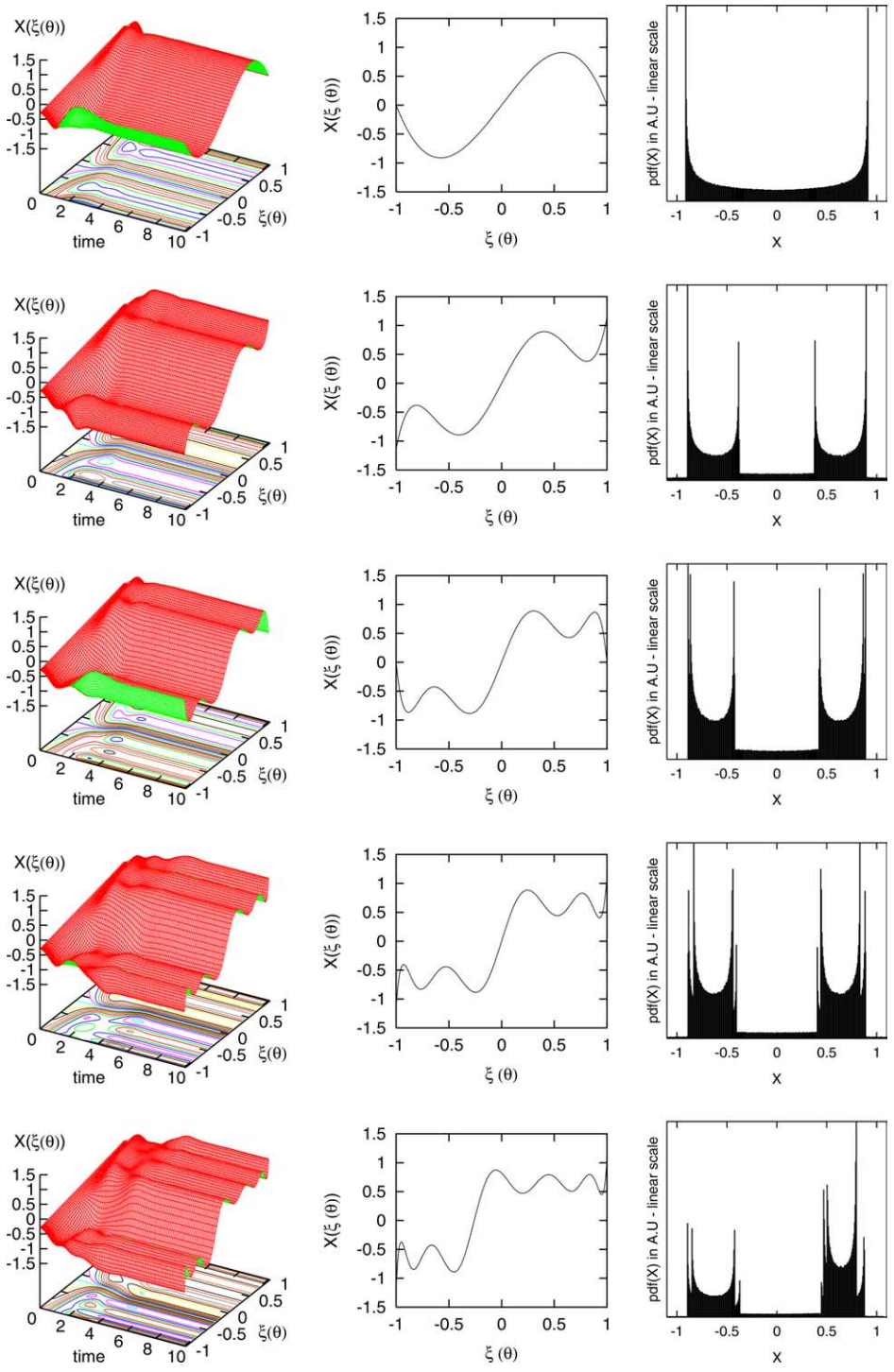

Fig. 2. Pseudo-spectral WLe solution for the model problem of Section 3.2.1. The left column shows the evolution of $X(t,\xi)$ for $0 \leqslant t \leqslant 10$. The solution $X(t=10)$ is plotted in the middle column and the steady-state pdf is shown in the right column. Results are obtained for expansion orders $N_o = 3$, 5, 7, 9 and 11, arranged from top to bottom.

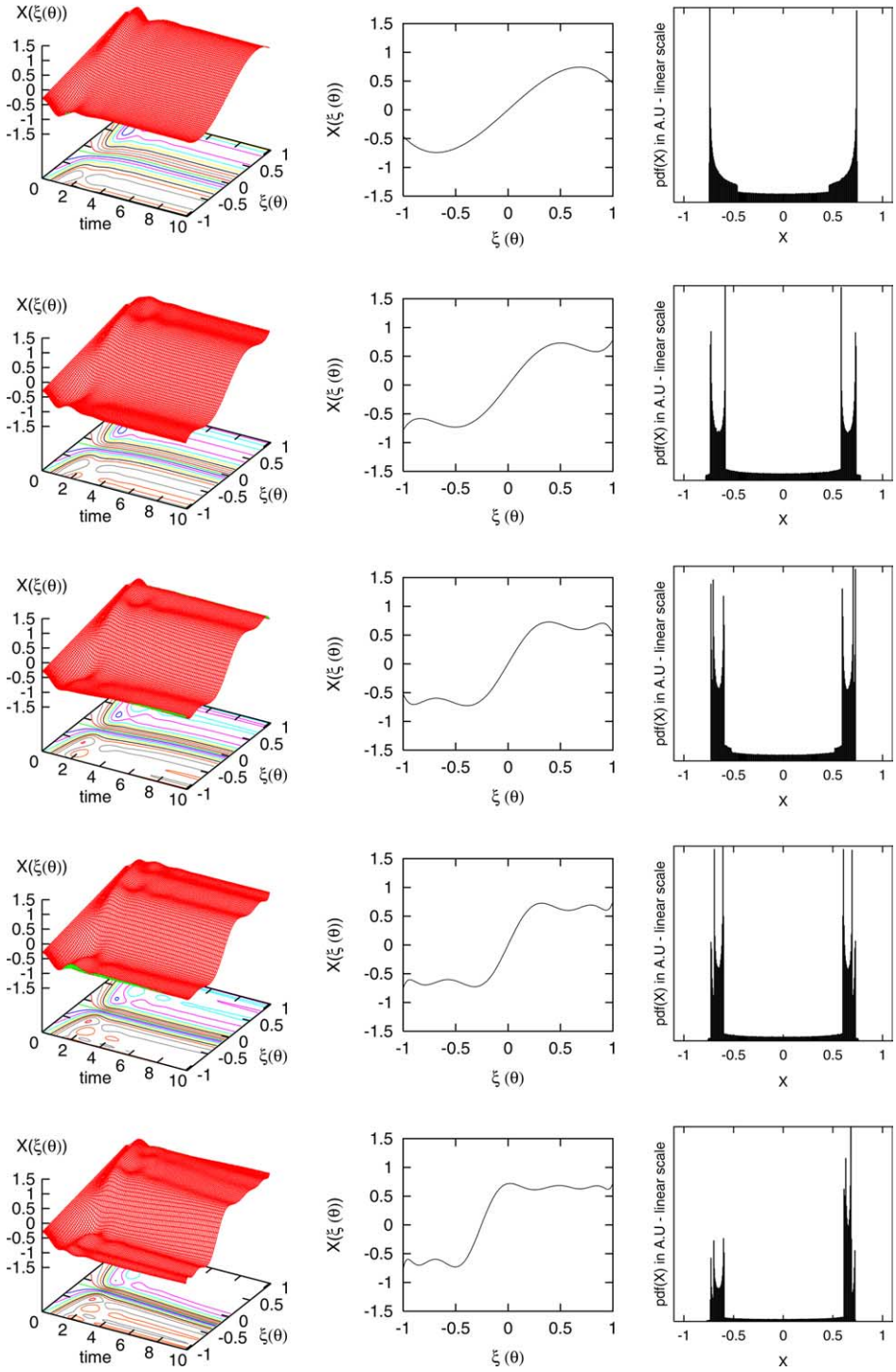

Fig. 3. Galerkin WLe solution for the model problem of Section 3.2.1. The left column shows the evolution of $X(t,\xi)$ for $0 \leqslant t \leqslant 10$. The solution $X(t = 10)$ is plotted in the middle column and the steady-state pdf is shown in the right column. Results are obtained for expansion orders $N_o = 3$, 5, 7, 9 and 11, arranged from top to bottom.

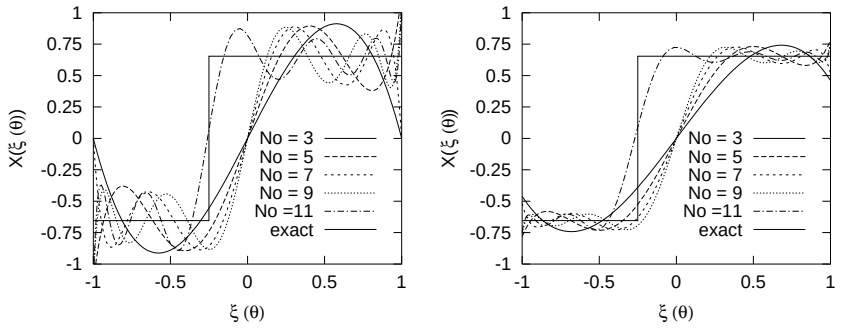

Fig. 4. Steady solution $X(t \to \infty)$ of the model problem of Section 3.2.1, obtained using WLe expansions with $N_o = 3$, 5, 7, 9 and 11. Plotted are curves obtained using a pseudo-spectral (left) and Galerkin (right) approximation.

with multiple peaks. This is also characteristic of the application of a spectral representation to a discontinuous problem.

In addition to poor representation of the process pdf, in the present case the WLe scheme also fails to provide accurate predictions of some of the low-order moments. To illustrate this claim, we provide in Fig. 5 the WLe predictions of the mean and SD of X at steady state for $N_o = 3, \ldots, 31$. The results demonstrate that the mean response is poorly estimated for both the Galerkin and pseudo-spectral approximations, and that it fluctuates substantially with N_o. Better, though still inadequate, predictions of the SD are obtained. Similar to the mean, these predictions also fluctuate with N_o.

3.2.2. WHa scheme

The WHa scheme is now applied to the same problem of Section 3.2.1. Results are obtained for an increasing number N_r of resolution levels. Fig. 6 shows the evolution of $X(t, \xi)$ for $0 \leqslant t \leqslant 10$; results obtained with $N_r = 2$, 3, 4 and 5 are depicted. The results indicate that, so long as $N_r > 2$, the WHa scheme correctly captures the bifurcation dividing the trajectories converging to the two stable equilibrium points. The transition is first captured at $N_r = 3$ and further increase of the value of N_r only affects the smoothness of the solution during the initial transient. For $N_r = 2$, the WHa scheme yields an incorrect result for $-0.5 \leqslant \xi \leqslant 0$, predicting in this range that the position rapidly equilibrates at $X = 0$. This corresponds to a physical but unstable equilibrium point. This erroneous prediction is obtained because the mean initial position over the corresponding uncertainty range is zero. It is interesting to note that, although the prediction for $N_r = 2$ is incorrect for $-0.5 \leqslant \xi \leqslant 0$, it is correct for the remaining parts of the uncertainty range. Thus, errors incurred at specific values of the random data do not appear to pollute the entire prediction; this (desirable) property of WHa schemes has been observed in a large number of (under-resolved) computations.

The mean and SD of X at steady state are reported in Table 1 for all considered values of N_r. We observe that for $N_r \geqslant 3$ the analytical prediction is exactly recovered. This complete agreement with the analytical solution is due to the fact that the discontinuity, located at $\xi = -0.25$, is "naturally" captured for $N_r \geqslant 3$; it is specifically located at the edge of neighboring wavelets at the level $j = 3$. Thus, the steady-state solution has vanishing details for scales (or resolution indices) $j > 3$.

3.2.3. Highly discontinuous solution

The example above showed that in the case of a single point of discontinuity, the WHa decomposition can provide an accurate representation of the stochastic process, but that the WLe scheme proved inadequate. To have a finer appreciation of the properties of the WHa scheme, we now consider a more difficult

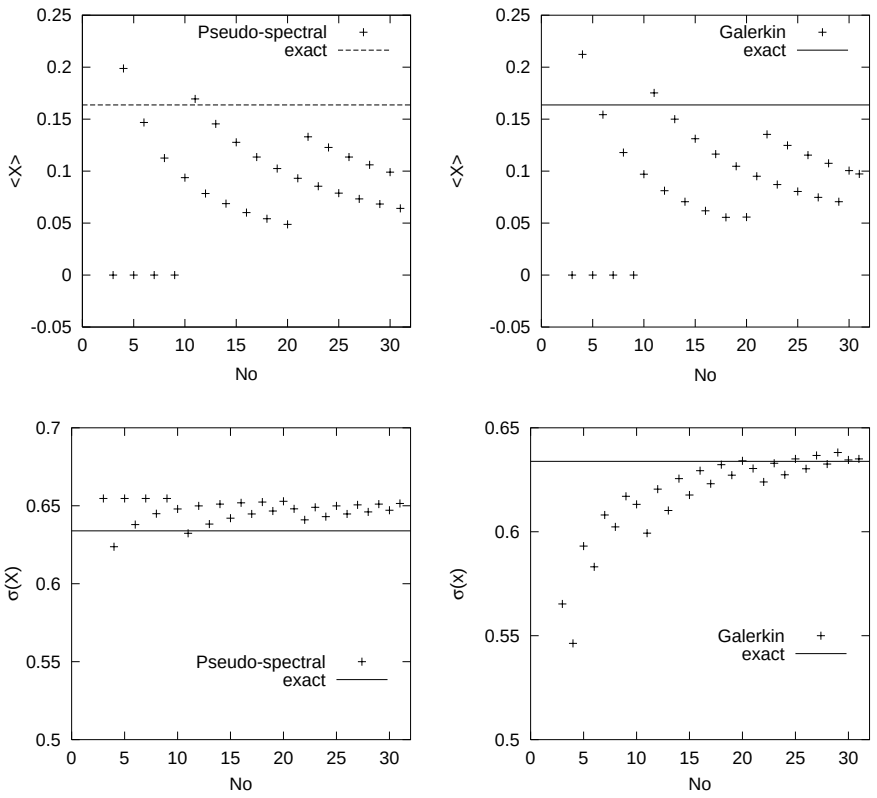

Fig. 5. Convergence with N_o of the computed mean (top) and SD (bottom) of $X(t \to \infty)$ using WLe expansion for the model problem of Section 3.2.1. Plotted are curves obtained using a pseudo-spectral (left) and Galerkin (right) approximation. The analytical predictions are given by $\langle X(\theta)\rangle = 0.16366$ and $\sigma(X(\theta)) = 0.63387$.

problem obtained simply by reducing the friction coefficient, f. Specifically, we set $f = 0.05$ and focus on stochastic initial conditions given by $X_0 = 1$ and $\Delta X = 0.1$. As in the previous case, the particle is released from a state of rest, i.e. the initial velocity is deterministic and equal to 0.

The reduction of the friction coefficient, together with the higher initial energy of the system, results in a complex response. Specifically, the particle oscillates for several cycles between the two potential wells, before reaching a final equilibrium position. Furthermore, the inverse map between each of two stable equilibrium points and the corresponding initial positions (which as previously mentioned is assumed to be uniformly distributed between 0.9 and 1.1) results in a union of several disjoint intervals. Thus, the situation is more complex than that of the previous problem, where two intervals were obtained. Consequently, one anticipates that a significantly higher resolution level would be needed to correctly characterize the behavior of the stochastic system.

To illustrate the convergence of the WHa scheme in the present case, results were obtained with a wider range of resolution levels, $3 \leqslant N_r \leqslant 8$. Results are plotted in Fig. 7, which depicts $X(\xi)$ at $t = 100$ for all considered values of N_r. The results indicate that for the present conditions, six resolution levels are needed to capture the response of the system, and particularly all the corresponding discontinuities. By increasing the resolution level beyond $N_r = 6$, one obtains additional details on the response of the system within the regions of continuity, as well as a slight refinement of the locations of the discontinuities.

One also notes that, even when the resolution level is too low to correctly capture all of the discontinuities, the WHa expansion still provides a meaningful prediction, in the sense that steady-state realizations

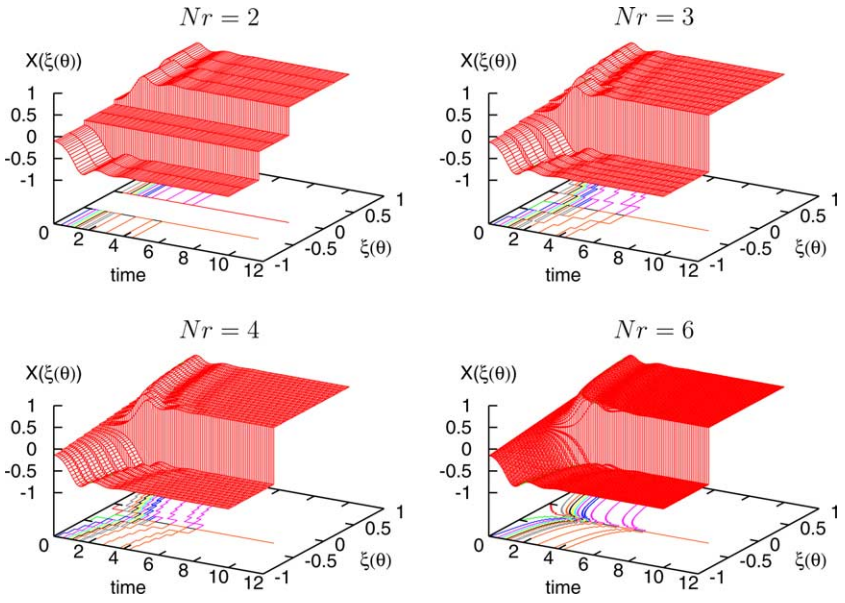

Fig. 6. WHa solution for the model problem of Section 3.2.2. The plots show the evolution of $X(t,\xi)$ for different resolution levels, $N_r = 2$, 3, 4 and 6.

Table 1
Mean and SD of X at steady state

N_r	$\langle X(\theta)\rangle$	$\sigma(X(\theta))$
2	0.3273268	0.566946718
3	0.1636634	0.633865691
4	0.1636634	0.633865691

Results are obtained using the WHa scheme with different N_r. The analytical predictions are give by $\langle X(\theta)\rangle = 0.1636634$ and $\sigma(X(\theta)) = 0.633865691$.

do in fact correspond to a stable equilibrium point. In other words, resolution errors do not lead to an unphysical prediction. This robustness of the WHa expansion is further illustrated in Fig. 8 which compares the WHa solution using $N_r = 7$ with the pseudo-spectral WLe prediction with $N_o = 32$. The results are generated at $t = 250$, where a stationary state is nearly reached. The figure shows that the pseudo-spectral WLe prediction is everywhere polluted by wiggles and yields predictions that are far from true equilibrium; meanwhile, the Galerkin WLe scheme predicts a constant solution $X(\xi) = \sqrt{15/35}$ (not shown). With the WHa scheme, on the other hand, the correct result is obtained. Naturally, the robustness of the WHa predictions should be carefully exploited, so as to ensure that the process is adequately resolved and that statistical moments are accurately computed. This can be achieved by systematic refinement of resolution level, as performed in the example above.

4. Application to Rayleigh–Bénard Instability

In the previous section, a simple model problem was considered whose motion is governed by a simple ODE. In this section, we address a more complex problem that consists of a stochastic Rayleigh–Bénard

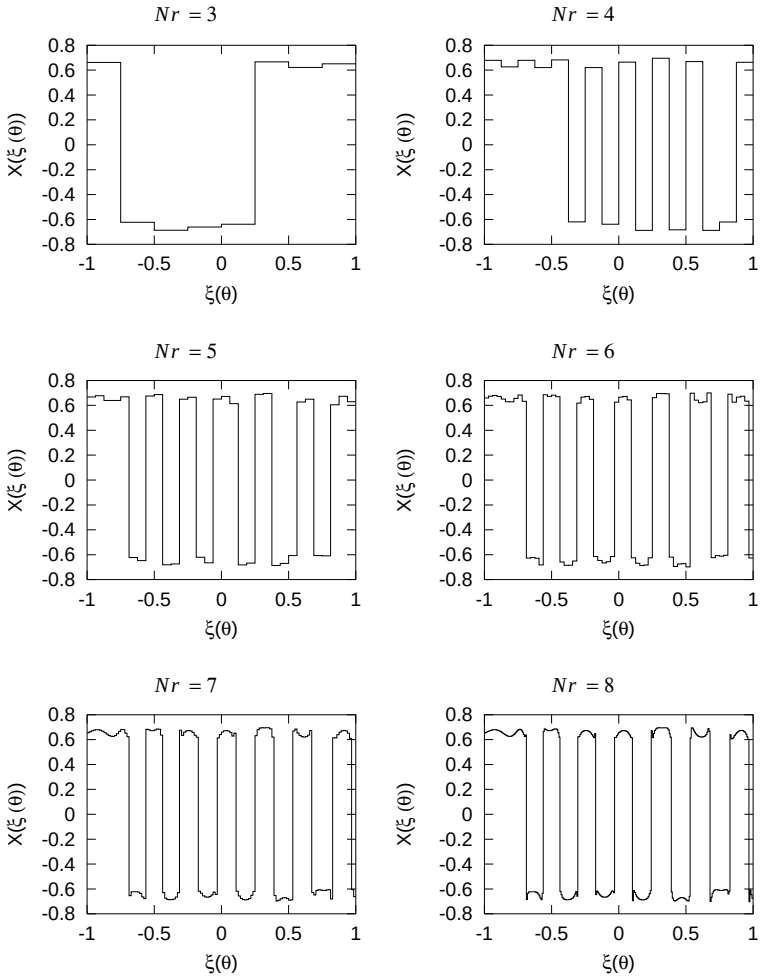

Fig. 7. WHa solution at $t = 100$ for the model problem of Section 3.2.3. The plots show curves of $X(t = 100, \xi)$ versus ξ, computed using different resolution levels, $N_r = 3$, 4, 5, 6, 7 and 8 as indicated.

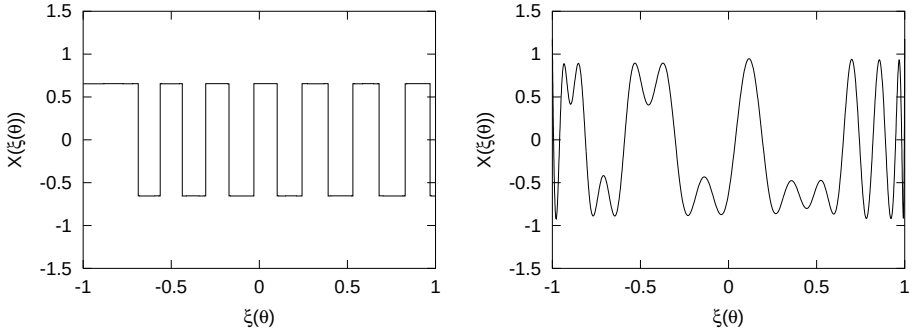

Fig. 8. Large-time (steady) solutions for the problem of Section 3.2.3. Plotted are curves for $X(t \to \infty, \xi)$ versus ξ. Left: WHa expansion with $N_r = 6$; right: pseudo-spectral WLe expansion with $N_o = 32$.

flow with random data in the neighborhood of the critical point. Specifically, we consider a closed rectangular 2D cavity of height H and length L that is filled with a Newtonian fluid. Gravity points downward, and the bottom wall of the cavity is maintained at a hot temperature T_{hot} while the top wall is maintained at a cold temperature T_{cold}. The vertical thermal gradient can also be characterized in terms of the reference temperature $T_{\text{ref}} \equiv (T_{\text{hot}} + T_{\text{cold}})/2$, and the temperature difference $\Delta T \equiv T_{\text{hot}} - T_{\text{cold}}$. The vertical walls are assumed to be adiabatic.

4.1. Deterministic system

Assuming that the temperature is difference small, i.e. $\Delta T/T_{\text{ref}} \ll 1$, the Boussinesq approximation is invoked. Thus, for deterministic conditions the flow is governed by the following system of normalized equations [29,30]:

$$\nabla \cdot \boldsymbol{u} = 0, \tag{29}$$

$$\frac{\partial \boldsymbol{u}}{\partial t} + \boldsymbol{u} \cdot \nabla \boldsymbol{u} = -\nabla p + \frac{Pr}{\sqrt{Ra}} \nabla^2 \boldsymbol{u} + Pr \Theta \boldsymbol{y}, \tag{30}$$

$$\frac{\partial \Theta}{\partial t} + \nabla \cdot (\boldsymbol{u}\Theta) = \frac{1}{\sqrt{Ra}} \nabla^2 \Theta, \tag{31}$$

where $\boldsymbol{u}$ is the velocity, p is the pressure, t is the time, and $\Theta \equiv (T - T_{\text{ref}})/\Delta T$ is the scaled temperature. The system involves two dimensionless parameters, namely the Prandtl number $Pr \equiv \mu c_{\text{p}}/\kappa$, and the Rayleigh number $Ra \equiv (\rho g \beta \Delta T H^3)/(\mu\kappa)$. Here, μ is the viscosity, c_{p} is the heat capacity, κ is the thermal conductivity, ρ is the density, g is the gravity, and β is the coefficient of thermal expansion.

Let Ω denote the computational domain, $\partial\Omega$ its boundary. We denote by $\partial\Omega_{\text{c}}$ the cold wall, $\partial\Omega_{\text{h}}$ the hot wall, and $\partial\Omega_{\text{v}}$ the vertical walls; we have $\partial\Omega = \partial\Omega_{\text{h}} \cup \partial\Omega_{\text{c}} \cup \partial\Omega_{\text{v}}$. Using this notation, the boundary conditions are expressed as

$$\boldsymbol{u}(\boldsymbol{x}, t) = 0 \quad \forall \boldsymbol{x} \in \partial\Omega, \quad \Theta(\boldsymbol{x}, t) \equiv \Theta_{\text{h}} = \frac{1}{2} \quad \forall \boldsymbol{x} \in \partial\Omega_{\text{h}}, \tag{32}$$

$$\Theta(\boldsymbol{x}, t) \equiv \Theta_{\text{c}} = -\frac{1}{2} \quad \forall \boldsymbol{x} \in \partial\Omega_{\text{c}}, \quad \frac{\partial \Theta(\boldsymbol{x}, t)}{\partial x} = 0 \quad \forall \boldsymbol{x} \in \partial\Omega_{\text{v}}. \tag{33}$$

The stability of the Rayleigh–Bénard problem summarized above has been extensively analyzed. In particular, results [31,32] reveal the existence of a critical value of Ra_{c} of the Rayleigh number, below which the flow is stable. In this regime, the fluid velocity vanishes identically, and the temperature distribution exhibits a linear variation vertically across the cavity, which is representative of a purely conductive system. Above the critical value, the flow is unstable and the growth of the instability leads to the establishment of recirculation zones, which results in enhanced heat transfer across the cavity.

Below, we address a stochastic variant of the Rayleigh–Bénard problem, focusing on the case of random parameter which can result in either stable or unstable flow behavior. The presence of the bifurcation provides a significant challenge to the computations. Below, we address this question by applying both the WLe and WHa expansions to the case of cavity with aspect ratio $A \equiv L/H = 2$, filled with air ($Pr = 0.7$), under deterministic cold-wall temperature T_{c} but random hot-wall temperature T_{h}. The statistics of T_{h} are assumed to be such that both stable and unstable behavior occur with finite probability.

4.2. Stochastic formulation

As mentioned above, the hot-wall temperature is now considered to be random. We model the uncertainty by decomposing Θ_h as $\Theta_h(\theta) \equiv \Theta_h(\xi(\theta)) = (1/2) + \Theta_r\xi(\theta)$. (In the stochastic case, the quantities ΔT and T_{ref} are defined using the mean hot-wall temperature, $\langle T_h \rangle$.) Thus, Θ_r characterizes the random fluctuations around the mean. The random variable ξ is assumed to be uniformly distributed on the interval $[-1, 1]$.

Similar to the approach of the previous section, both the WLe and WHa expansions are implemented. Thus, in the former case the solution is represented in terms of Legendre polynomials $\mathscr{L}e_k$, and in the latter in terms of Haar wavelets, $\mathscr{H}a_k$. We shall derive the governing equations in terms of a generic basis $\Psi_k,\ k = 0, \ldots, P$, where $P + 1$ is the dimension of the basis and Ψ_k denotes either $\mathscr{L}e_k$ or $\mathscr{H}a_k$. Using this notation, the uncertain velocity, pressure and temperature fields are expanded as

$$\boldsymbol{u}(\boldsymbol{x}, t, \xi) = \sum_{k=0}^{P} \Psi_k(\xi)\boldsymbol{u}_k(\boldsymbol{x}, t), \tag{34}$$

$$p(\boldsymbol{x}, t, \xi) = \sum_{k=0}^{P} \Psi_k(\xi)p_k(\boldsymbol{x}, t), \tag{35}$$

$$\Theta(\boldsymbol{x}, t, \xi) = \sum_{k=0}^{P} \Psi_k(\xi)\Theta_k(\boldsymbol{x}, t). \tag{36}$$

Governing equations for the unknown coefficients are obtained by introducing these expansions into the governing equations, multiplying the result by Ψ_i and evaluating the expectation. Exploiting the orthogonality of the basis, we obtain the following coupled system [12,13]:

$$\nabla \cdot \boldsymbol{u}_i = 0, \tag{37}$$

$$\frac{\partial \boldsymbol{u}_i}{\partial t} + \sum_{j=0}^{P}\sum_{k=0}^{l} \mathscr{M}_{ijk}\boldsymbol{u}_j \cdot \nabla \boldsymbol{u}_k = -\nabla p_i + \frac{Pr}{\sqrt{Ra}}\nabla^2 \boldsymbol{u}_i + Pr\Theta_i \boldsymbol{y}, \tag{38}$$

$$\frac{\partial \Theta_i}{\partial t} + \sum_{j=0}^{P}\sum_{k=0}^{l} \mathscr{M}_{ijk}\nabla \cdot (\boldsymbol{u}_j\Theta_k) = \frac{1}{\sqrt{Ra}}\nabla^2\Theta_i \tag{39}$$

for $i = 0, \ldots, P$. Here, $\mathscr{M}$ is the multiplication tensor, given by

$$\mathscr{M}_{ilm} = \mathscr{M}_{iml} \equiv \frac{\langle \Psi_i\Psi_j\Psi_k \rangle}{\langle \Psi_i\Psi_i \rangle}.$$

Velocity boundary conditions on $\partial\Omega$ are $\boldsymbol{u}_i = 0$ for $i = 0, \ldots, P$. For the scaled temperature, we have

$$\Theta_0 = -\frac{1}{2}, \quad \Theta_{i=1,\ldots,P} = 0 \quad \forall \boldsymbol{x} \in \partial\Omega_c, \tag{40}$$

$$\Theta_i = \frac{\langle \Theta_h(\xi)\Psi_i(\xi)) \rangle}{\langle \Psi_i\Psi_i \rangle} \quad \text{for } i = 0, \ldots, P \ \forall \boldsymbol{x} \in \partial\Omega_h, \tag{41}$$

$$\frac{\partial \Theta_i}{\partial x} = 0 \quad \text{for } i = 0, \ldots, P \ \forall \boldsymbol{x} \in \partial\Omega_{\mathrm{v}}. \tag{42}$$

4.2.1. Numerical method and baseline results

The governing equations (37)–(39) are integrated using the stochastic projection method (SPM) described in [13]. The method relies on a second-order, conservative, finite-difference discretization of field variables. Velocities are discretized on cell edges, while pressure and temperature are discretized at cell centers. Velocity divergence constraints are efficiently implemented using a pressure correction step, which involves the solution of a system of decoupled pressure Poisson equations [12]. The present construction generalizes the scheme developed in [13], primarily by incorporation an extended formulation that adapts the multiplication tensor to the selected basis function expansion.

Prior to performing stochastic simulations, deterministic computations were performed (simply by setting $P = 0$). We set $Ra = 2150$, i.e. the Rayleigh number is slightly larger than critical. The simulations were then performed by perturbing the hot-wall temperature so as to determine the critical conditions for the instability. In these computations, the initial condition consists of the purely conductive solution, which is perturbed using a low-energy white-noise perturbation. As illustrated in Fig. 9, after a short time the kinetic energy exhibits an exponential growth or decay, depending on the (perturbed) value of the hot-wall temperature. The critical temperature is determined by computing the growth rate for different values of Θ_{h}, as shown in Fig. 9. The curve is then interpolated in order to locate the value where the growth rate vanishes. The results indicate that, for the present parameters, a critical value $\tilde{\Theta}_{\mathrm{h}} = 0.4301$ is obtained.

Consequently, for the presently selected conditions, the overall heat transfer corresponds to the purely conductive solution whenever $\Theta_{\mathrm{h}} \leqslant \tilde{\Theta}_{\mathrm{h}}$. The rate of heat transfer is characterized using the Nusselt number:

$$Nu \equiv \frac{1}{A(\Theta_{\mathrm{h}} - \Theta_{\mathrm{c}})} \int_0^A \left. \frac{\partial \Theta}{\partial y} \right|_{y=0} \mathrm{d}x.$$

Clearly, in the stable (conductive) regime, $Nu = 1$. For $\Theta_{\mathrm{h}} > \tilde{\Theta}_{\mathrm{h}}$, heat transfer enhancement occurs so that $Nu(\Theta_{\mathrm{h}}) > 1$. Thus, the difference $\delta Nu(\Theta_{\mathrm{h}}) \equiv Nu(\Theta_{\mathrm{h}}) - 1$ provides a measure of the heat transfer enhancement.

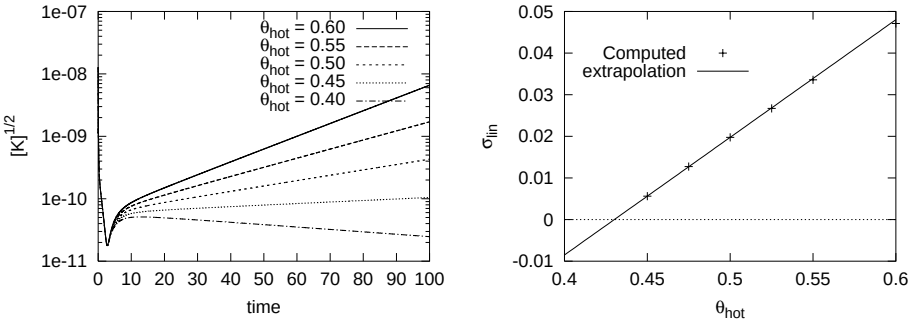

Fig. 9. Left: square root of kinetic energy versus time for the linearized Rayleigh–Bénard problem. Plotted are curves for different hot-wall temperatures. Right: linear growth rate versus hot-wall temperature. The critical value, determined by linear extrapolation, is $\tilde{\Theta}_{\mathrm{h}} = 0.4301$. The computations were performed on a uniform mesh having having 60 grid points in the x-direction and 30 grid points in the y-direction.

4.3. WLe expansion

In this section, we apply the WLe scheme to simulate the response of the stochastic flow. As mentioned earlier, we focus on the case of uncertain hot-wall temperature, which is assumed to be uniformly distributed in the range $[0.3, 0.5]$. Following the discussion above, both a stable and an unstable flow behavior occur for this uncertainty range.

Fig. 10 shows kinetic energy as a function of Θ_h for different values of N_o. The curves are reconstructed from the steady-state WLe coefficients. The results indicate that the curves approach each other as N_o increases, which suggests that the WLe computations are converging. Unfortunately, individual realizations obtained for $\Theta_h < \tilde{\Theta}_h$ do not exhibit a vanishing kinetic energy, as one would expect based on the stability considerations above. In other words, if the WLe computations are in fact converging, they do not appear to be converging to the exact solution.

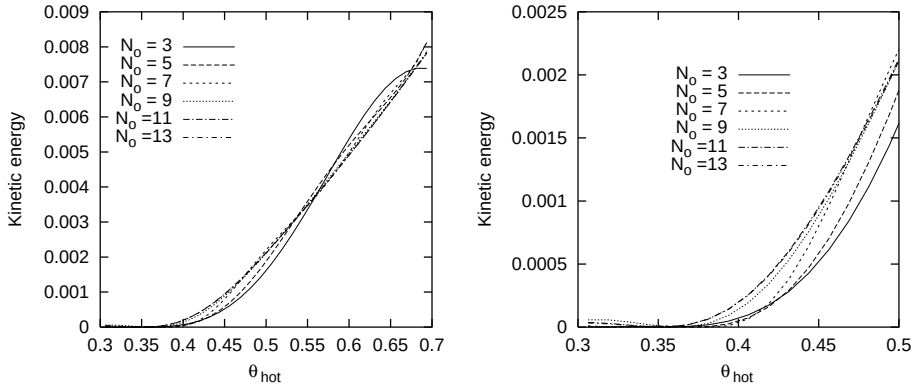

Fig. 10. Steady-state kinetic energy versus hot-wall temperature using WLe expansions with $N_o = 3$, 5, 7, 9, 11 and 13. The right plot shows a detailed view in the neighborhood of the critical value.

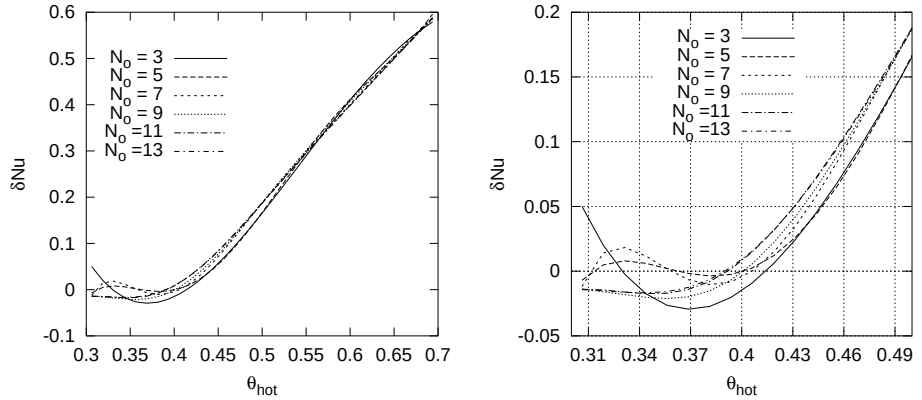

Fig. 11. $\delta Nu(\Theta_h)$ versus Θ_h using WLe expansions with $N_o = 3$, 5, 7, 9, 11 and 13. The right plot shows a detailed view in the neighborhood of the critical value.

In order to gain additional insight into the behavior of WLe predictions, we plot in Fig. 11 curves for δNu as function of $\Theta_h(\xi)$. As before; results are generated for different expansion orders, N_o. As for the kinetic energy, the observed behavior of δNu appears to converge with increasing N_o, but not to the exact solution. Furthermore, at low values of Θ_h, an unphysical effect, corresponding to negative values of δNu, can be observed. Specifically, the negative values of δNu indicate that, for the corresponding realizations, an overall heat transfer rate is predicted that is *smaller* than that of the conductive solution! This unphysical response occurs over a substantial band of possible realizations, which extends over about 25% of the entire range of possible realizations. The origin of the unphysical response is further analyzed in Fig. 12, which shows the steady-state velocity and temperature fields (reconstructed from the WLe expansion) for selected values of Θ_h. In particular, the figure shows that for sub-critical values of Θ_h, instead of vanishing, the predicted velocity exhibits a recirculating flow pattern with a *reverse* sign. Thus, the "energy leakage" that was earlier observed in Fig. 10 for small Θ_h is accompanied by a severe breakdown of the WLe prediction.

Fig. 13 shows the pdf of δNu for WLe expansion with $N_o = 3$, 5, 7 and 9. The results illustrate the difficulties of the computations in approaching the exact solution, which should exhibit a singular spike at $\delta Nu = 0$. Another symptom of the inefficiency of the WLe expansion for the present problem is the loss of

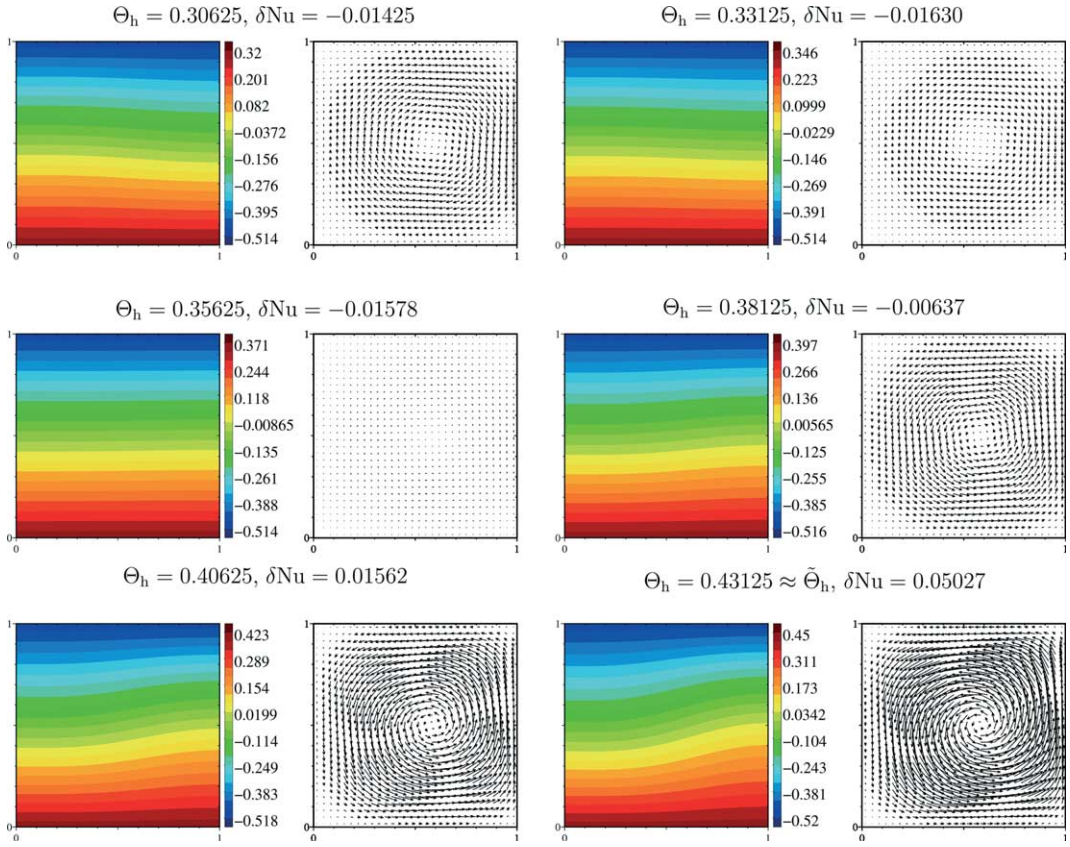

Fig. 12. Individual realizations of the steady-state temperature and velocity distributions, as predicted using a WLe expansion with $N_o = 9$. The selected values of Θ_h are indicated. Due to symmetry with respect to the mid vertical plane, only the left half of the cavity is plotted.

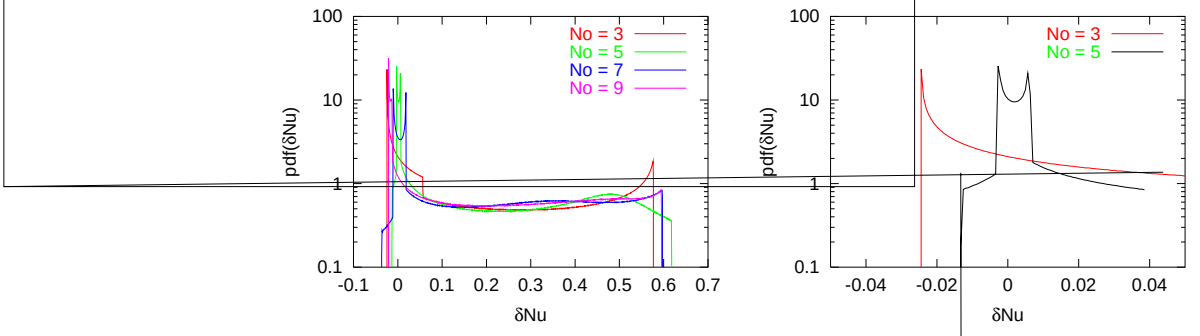

spectral convergence. This can be appreciated from Table 2, which provides the mean values of overall heat transfer rate, $\langle \int_0^A \partial\Theta/\partial y \, dx \rangle$, and of the corresponding SD for different N_o.

The present experiences indicate that for problems involving bifurcations or loss of smoothness with respect to the random data, the WLe expansion may be essentially impractical. Similar limitations are expected for other spectral representations [20] based on global basis functions.

4.4. WHa expansion

In this section, we apply the WHa scheme to compute the stochastic, steady-state response of the Rayleigh–Bénard flow. We use the same parameters as in the previous section, i.e. we focus on the case of uncertain hot-wall temperature. We start by examining global properties of the flow field, and then analyze stochastic velocity and temperature distributions.

4.4.1. Kinetic energy and heat transfer

Fig. 14 provides curves of the kinetic energy and δNu plotted against Θ_h. The curves are reconstructed based on the wavelet coefficients, and results are shown for expansion using $N_r = 2$, 3, 4 and 5. As far as these integral measures are concerned, the results indicate that the WHa scheme is much better adapted than the WLe scheme at capturing the transition between conductive and convective regimes, even when a coarse stochastic discretization with $N_r = 2$ is considered. As N_r increases, the computations provide an increasingly accurate estimate of the location of the critical point, as illustrated in Fig. 15. The latter provides an enlarged view of the local behavior of $\delta Nu(\Theta)$ near the critical point, as well as the dependence of δNu on ξ. In the latter format, the results illustrate the piecewise constant nature of the WHa expansion, as well as the essential concept of the approximation scheme which relies on projecting the solution onto the

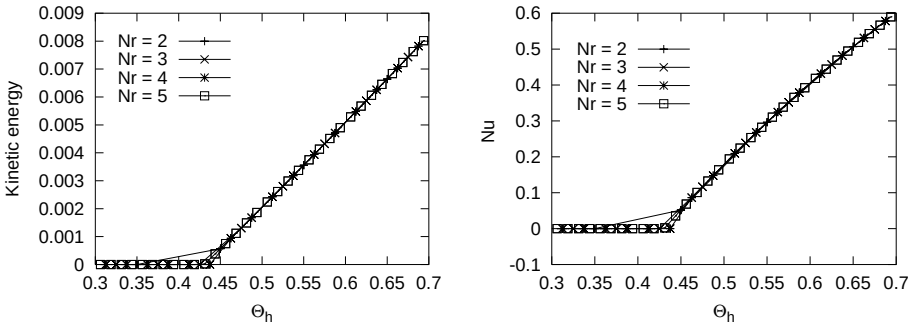

Fig. 14. Kinetic energy (left) and $\delta Nu(\Theta_h)$ (right) versus hot-wall temperature using WHa expansions with $N_r = 2$, 3, 4 and 5.

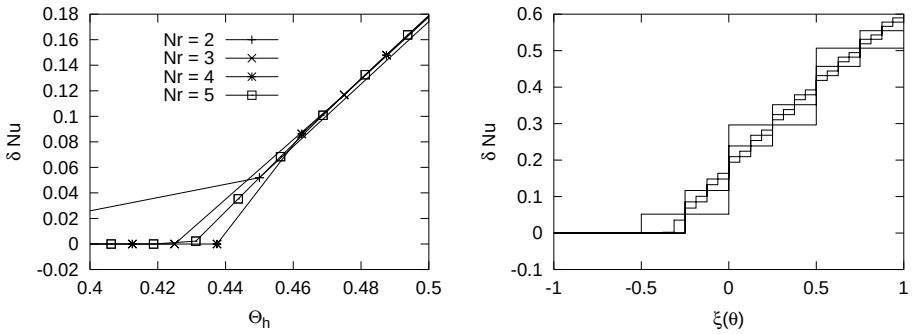

Fig. 15. Left: detailed view of δNu versus Θ_h in the neighborhood of the critical value. Right: detailed view of δNu versus ξ near the critical value. Plotted are curves obtained using WHa expansions with $N_r = 2$, 3, 4 and 5.

space V^{N_r}. The robustness of the WHa expansion in capturing the bifurcation can be appreciated by noting that the reconstructed curves capture the correct behavior on both sides of the critical point. Specifically, as predicted by the theory and confirmed by the perturbation analysis above, vanishing values of the kinetic energy and of δNu are predicted for subcritical values of Θ_h, while for supercritical values, an essentially linear increase of δNu with Θ_h is observed.

To gain further appreciation of the robustness of the WHa scheme, Table 3 provides the mean values of the overall heat transfer rate, $\langle \int_0^A \partial\Theta/\partial y \, dx \rangle$, and of the corresponding SD for different N_r. The results indicate that the predictions are close to one another and tend to cluster as N_r increases.

Table 3
Mean and SD of the overall heat transfer rate across the cavity

N_r	$\langle \int_0^A \partial\Theta/\partial y \, dx \rangle$	SD
1	2.22300	0.4230
2	2.23588	0.4524
3	2.23791	0.4627
4	2.23795	0.4653
5	2.23906	0.4652

Shown are results obtained using the WHa expansion with different resolution levels, N_r.

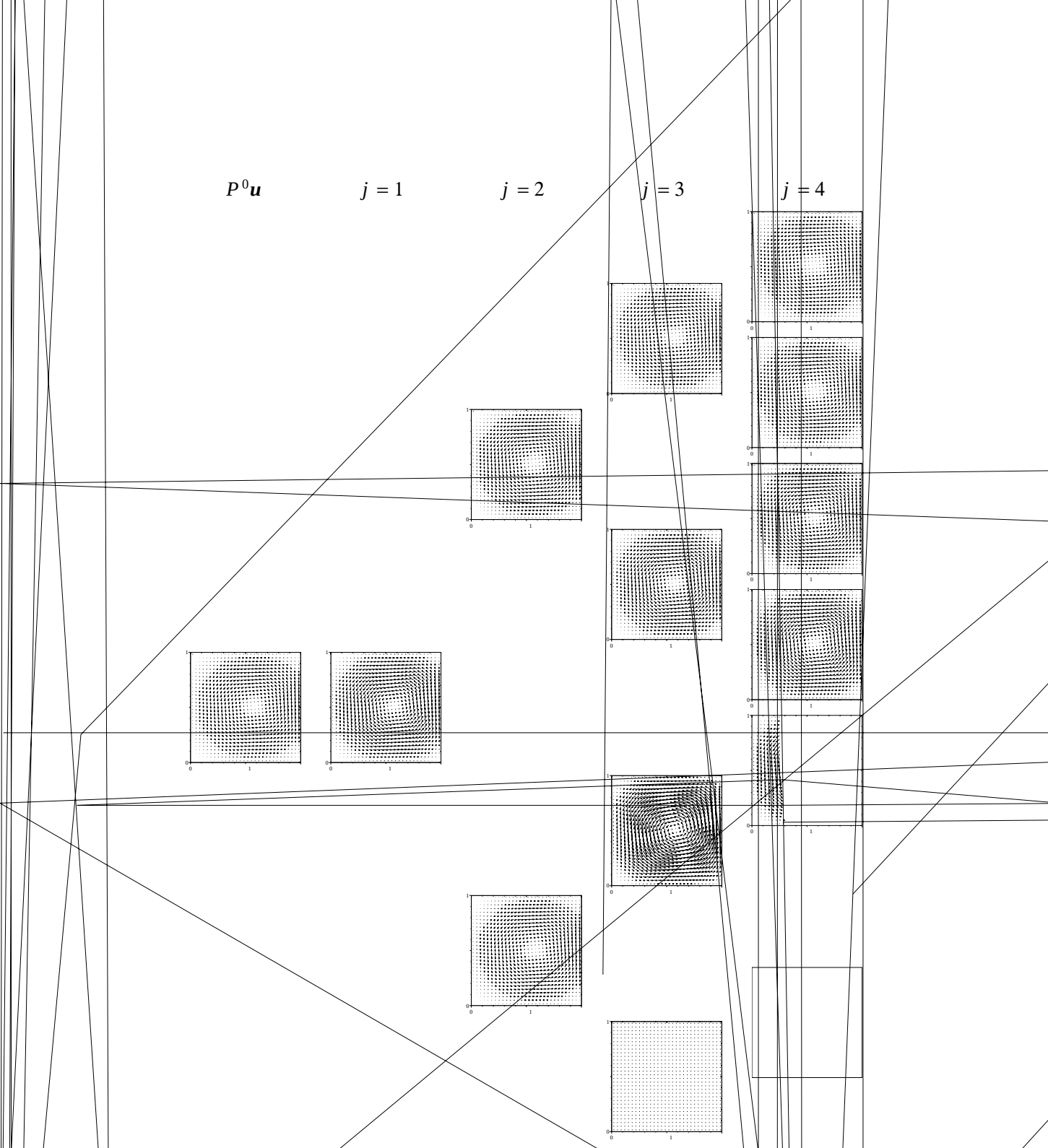

Fig. 16. Mean velocity field ($P\,\boldsymbol{u}$, left) and first wavelet modes, $\boldsymbol{u}_{j,k}$ using a WHaexpansion with N_r 5. The scale indices, j, are $^{j-1} - 1$ are plotted, and are arranged from bottom totop.

The magnitude of the vector is normalized using a factor equal to 2^{j+1}

4.4.2. Detail distributions of velocity and temperature

Fig. 16 shows the computed velocity fields corresponding to the detail coefficients. Recall that for the present 1D WHa expansion, the velocity is expressed in terms of the details $\boldsymbol{u}_{j,k}$ according to

$$\boldsymbol{u}(\boldsymbol{x},\xi) = \sum_{k=0}^{2^{N_r}-1} \boldsymbol{u}_k(\boldsymbol{x})\mathscr{H}a_k(\xi) \equiv \boldsymbol{u}_0 + \sum_{j=1}^{N_r}\sum_{k=0}^{2^{j-1}-1} \boldsymbol{u}_{j,k}\psi^{\mathrm{w}}_{j,k}(\mathrm{p}(\xi)).$$

In the left column of Fig. 16, we show the mean field $\boldsymbol{u}_0(\boldsymbol{x}) \equiv \langle \boldsymbol{u} \rangle$; in the second column, the detail corresponding to the difference of the mean with $P^1\boldsymbol{u}$. As expected, the latter indicates that the circulation inside the cavity increases with ξ, and accordingly with Θ_{h}. The second detail fields, which are plotted in the third column, correspond to differences between $P^2\boldsymbol{u}$ and $P^1\boldsymbol{u}$; they reveal a similar recirculating pattern as the first detail and point to a similar trend. More interesting trends can be observed from the detail fields at the next level, $j = 3$. Specifically, while the details corresponding to the highest values of Θ_{h} (appearing on top) exhibit similar patterns and trends as those for $j = 2$ and $j = 1$, those corresponding to the low values have different structure. Specifically, for $k = 0$, the field vanishes, indicating that no correction is needed for the corresponding "realizations". Furthermore, the detail for $k = 1$ has larger magnitude than the other details at the same level; this increased "activity" coincides with the location of the transition between conductive and convective regimes. On the next detail level, we again observe that no corrections are needed for the velocity fields at the lowest two temperature bands, whereas the corrections corresponding to the remaining fields reflect a trend of increasing circulation with higher temperatures. Similar trends can be observed by inspections of the details at the last level ($j = 5$), which are shown in Fig. 17.

The stochastic temperature field is analyzed following the same approach used for the velocity. In Fig. 18, we plot distributions of the mean velocity as well as the details for levels $j = 1$, 2, 3 and 4; details at the highest level, $j = 5$, are plotted in Fig. 19. Note that, unlike the velocity field, the detail distributions for temperature do not vanish, even at the highest resolution level. This is the case because inhomogeneous boundary conditions prevail at the hot wall, regardless of whether the flow is stable or not. Nonetheless, the transition from a conductive to a convective regime can still be detected. In the former case, the distributions are characterized by parallel horizontal contour lines while severe distortions of this pattern occur as the flow transitions. As for the velocity field, the results indicate that the transition is first captured at $j = 3$; at this level, the detail corresponding to $k = 0$ exhibits flat horizontal contours, while the detail temperature fields for $k > 0$ exhibit a distorted pattern that is characteristic of a recirculating flow field. It is interesting to note that at higher levels (Figs. 18 and 19), the detail distributions corresponding to supercritical temperature values exhibit a similar spatial distribution. This suggests that in this situation the higher levels primarily introduce an amplitude correction to the prevailing recirculating flow.

4.5. Continuous problem

The results of the previous sections demonstrate that the WHa expansion provides a robust and well-suited approach for analyzing stochastic processes involving bifurcations or discontinuous dependence on the random data. On the other hand, when the process depends smoothly on the random data, global spectral expansions are expected to be substantially more efficient than wavelet representations [21]. Specifically, for spectral representations a fast, "infinite-order" convergence is expected, while for the Haar representation errors are expected to decay as the inverse of N_{r}.

We briefly illustrate the convergence of the WHa and WLe schemes for a problem involving a smooth dependence on the random data. To this end, we consider once again the same stochastic Rayleigh–Bénard problem, but increase the Rayleigh number to $Ra = 3000$. For this value of the Rayleigh number, the convective regime always prevails as all possible realizations of Θ_{h} are larger than the critical value.

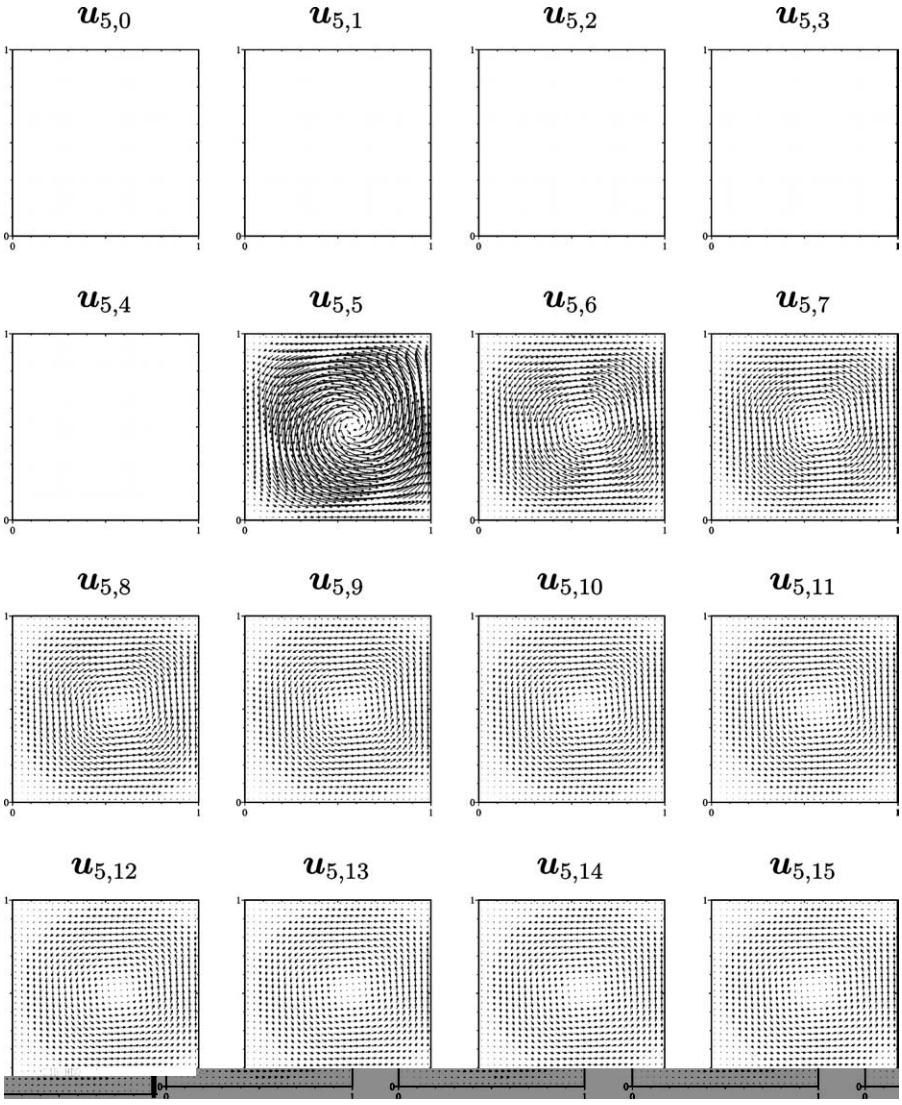

Fig. 17. Wavelet modes for the velocity field at a scale index $j = 5$. The magnitude of the vector is normalized using a factor equal to 2^{j+1}. Results are obtained using a WHa expansion with $N_r = 5$. The space index k is indicated, and only the left half of the cavity is plotted.

Table 4 shows predictions of the mean overall heat transfer and of the corresponding SD, using the WHa scheme with increasing N_r and the WLe scheme with increasing N_o. The results indicate that the WLe predictions rapidly become independent of N_o; in particular, identical predictions of the mean heat transfer and its SD are obtained with $N_o = 4$ and 5. The WHa predictions also appear to be converging as N_r increases, though at an appreciably smaller rate. To gain additional insight into the convergence of both predictions, we plot in Fig. 20 an approximate error estimate, defined as the absolute value of the difference between a given prediction and the WLe result with $N_o = 5$. Thus, in these estimates, the

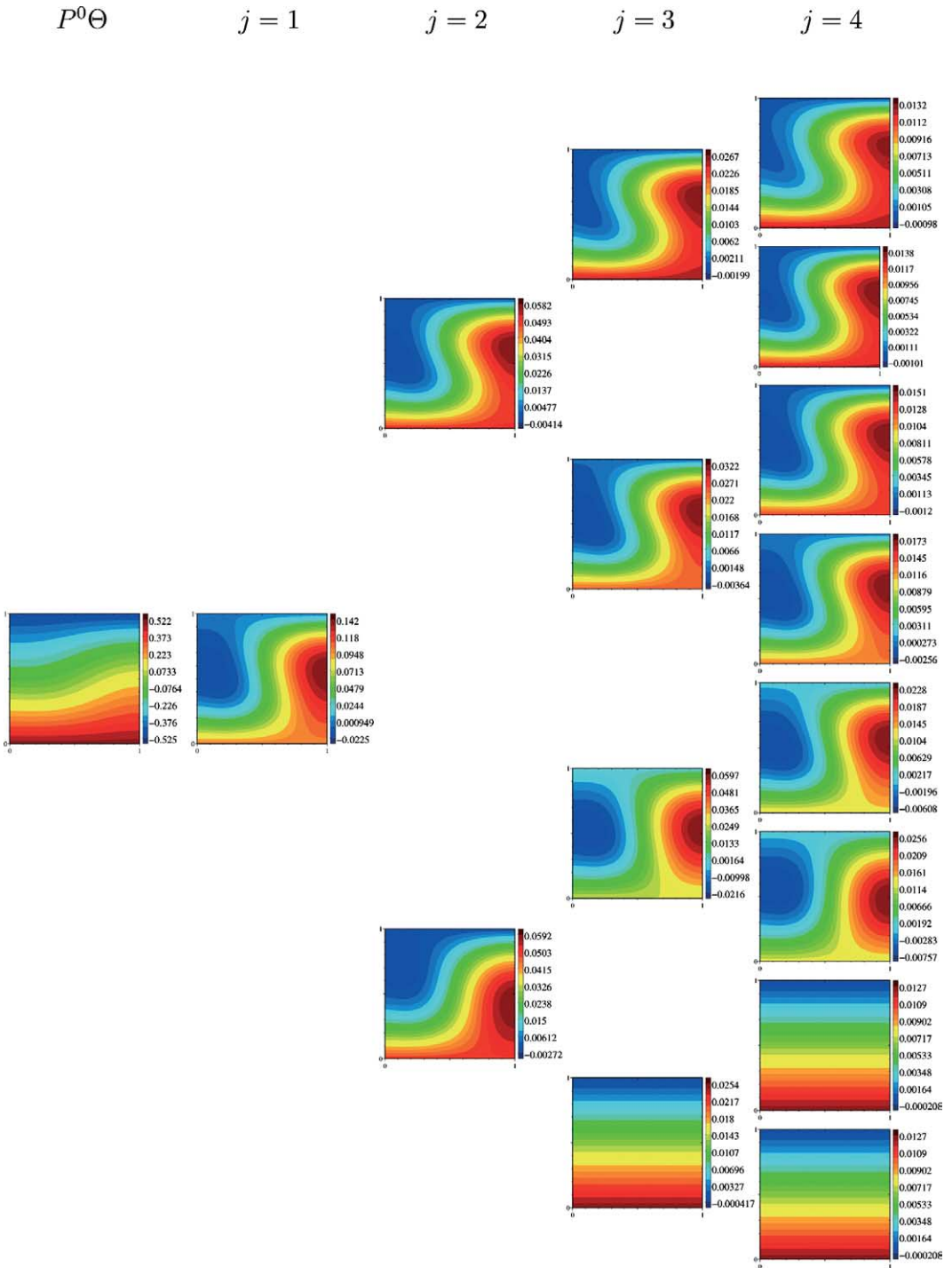

Fig. 18. Mean temperature field ($P^0\Theta$, left) and first wavelet modes, $\Theta_{j,k}$ using a WHa expansion with $N_r = 5$. The scale indices, j, are indicated. At each scale index, frames for different space indices $k = 0, \ldots, 2^{j-1} - 1$ are plotted, and are arranged from bottom to top. Due to symmetry with respect to the mid vertical plane, only the left half of the cavity is plotted.

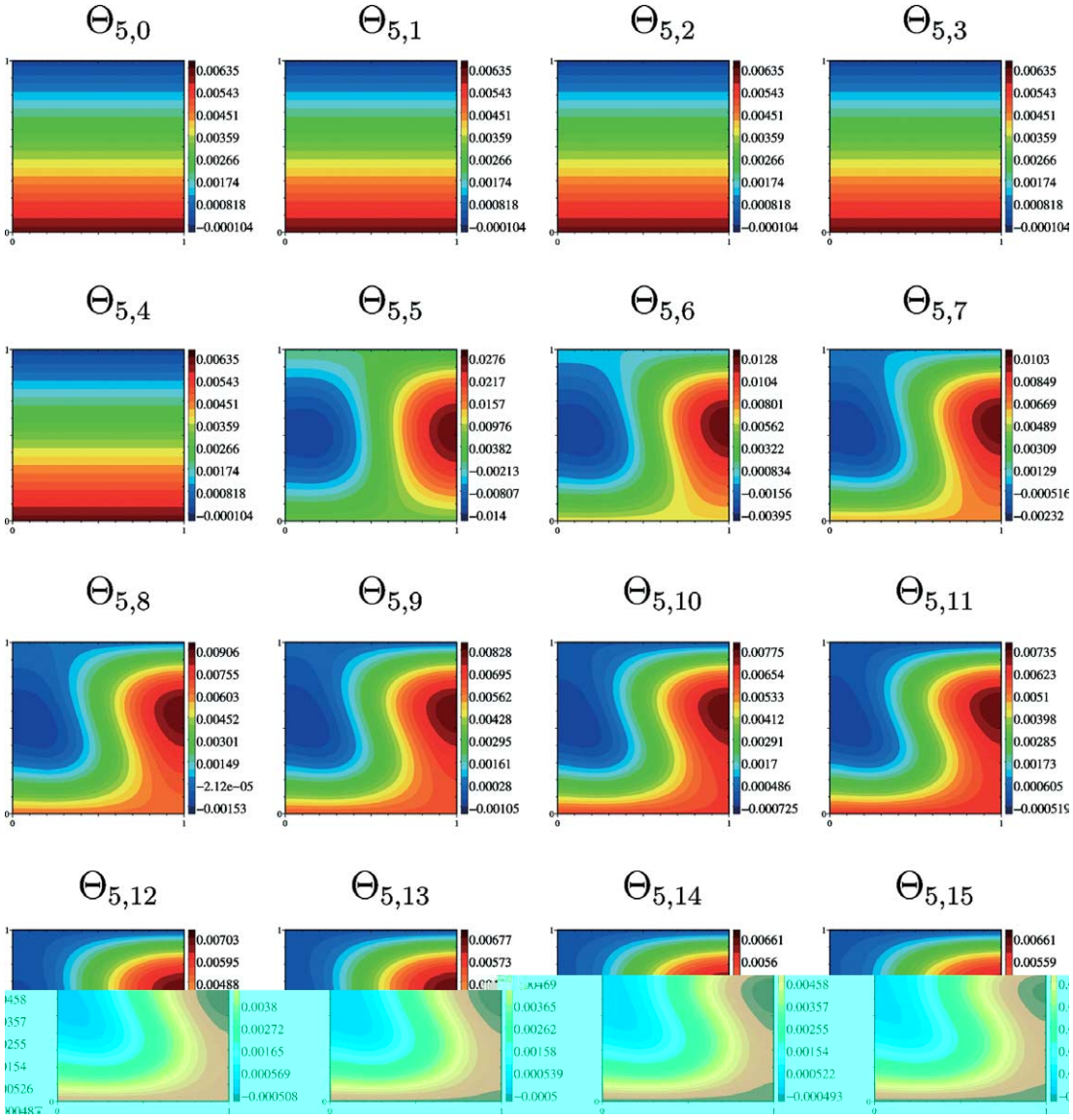

Fig. 19. Wavelet modes for the temperature field at a scale index $j = 5$. Results are obtained using a WHa expansion with $N_r = 5$. The space index k is indicated, and only the left half of the cavity is plotted.

fifth-order WLe solution is used as surrogate for the exact solution. The results of Fig. 20 illustrate the fast decay of the error for the WLe scheme. For the WHa scheme, the error also decays with increasing N_r, though at an appreciably smaller rate. The moderate rate of convergence of the WHa computations can also be appreciated in Fig. 21, which depicts the computed distributions of δNu for different values of N_r. The results illustrate the "staircase" Haar approximation of the continuous curve expressing the dependence of δNu on Θ_h and on ξ. Thus, for the present conditions, the WLe scheme outperforms the WHa scheme.

Table 4
Mean and SD of the overall heat transfer rate across the cavity

	$\langle \int_0^A \partial\Theta/\partial y \, dx \rangle$	SD
N_r		
1	2.92239879	0.49257723
2	2.92350067	0.55054599
3	2.92377786	0.56409585
4	2.92384732	0.56743188
5	2.92386463	0.56826288
6	2.92386897	0.56847041
N_o		
1	2.92384455	0.56871803
2	2.92387023	0.56854003
3	2.92387042	0.56853954
4	2.92387042	0.56853957
5	2.92387042	0.56853957

Shown are results obtained using the WHa expansion with different resolution levels, N_r, and the WLe scheme with different values of N_o. The Rayleigh number $Ra = 3000$, and unstable conditions prevail for all possible realizations of the hot-wall temperature.

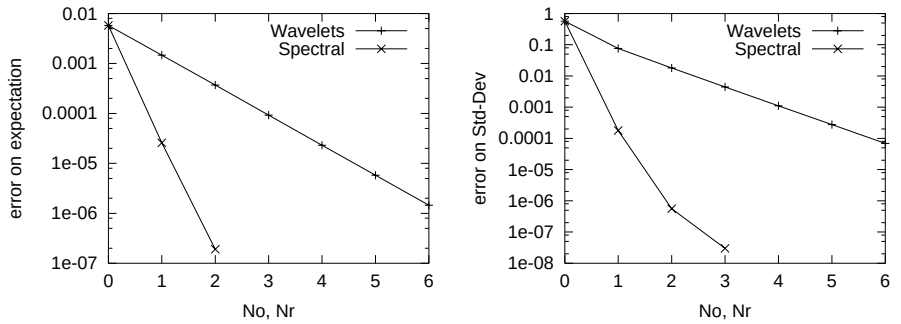

Fig. 20. Convergence of the expected (left) and SD (right) of Nu with increasing N_o for the WLe expansion and N_r for the WHa expansion. The errors is estimated using the absolute value of the difference between the solution and the WLe prediction with $N_o = 5$.

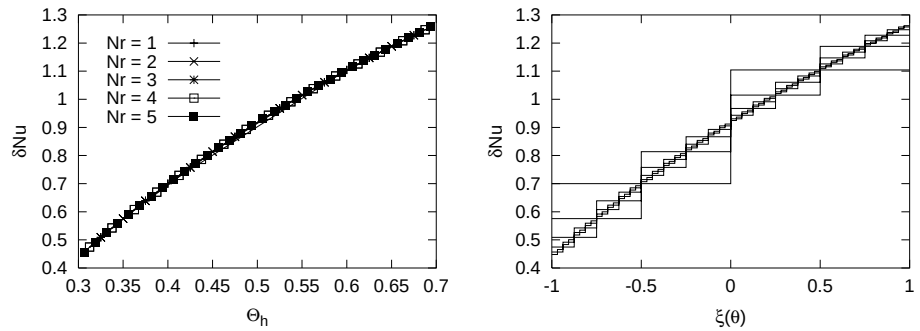

Fig. 21. δNu versus Θ_h (left) and versus ξ (right) using WHa expansions with $N_r = 1, 2, 3, 4$ and 5.

5. Conclusions

In this paper, an uncertainty propagation scheme is constructed based on generalized PC representations. The scheme relies on an orthogonal representation of the dependence of the solution on random parameters. A spectral representation in terms of Legendre basis functions is considered, as well as an orthogonal decomposition using Haar wavelets. In both cases, the unknown coefficients in the expansion are evaluated using a Galerkin procedure, which results in coupled evolution equations for the stochastic modes. The behavior of the resulting schemes is analyzed in light of computations of a simple dynamical system, and of simulations of near-critical Rayleigh–Bénard flow. In both cases, attention is focused on the case of a steep or discontinuous dependence of the stochastic process on the random input data.

The model computations focused on the idealized case of a particle moving under the action of an imposed potential and friction. Randomness is introduced in the form of a stochastic initial position, with uniform probability between two specified bounds. Depending on the value of the friction coefficient, the random process admits single or multiple discontinuities. When a single discontinuity occurs, the steady behavior of the problem was characterized analytically, and the analytical solution is used to verify computed predictions. The results indicate that the WHa scheme is well adapted to the present situation, and that the steady-state analytical predictions are recovered when sufficient resolution is provided. In contrast, computations performed using a WLe expansion provided poor estimates of both low-order statistics and of individual realizations. The robust behavior of the WHa scheme was also verified in situations where the stochastic system admits multiple discontinuities with respect to the random data. As in the previous case, the results indicate that, with sufficient resolution, accurate estimates of the statistics and of individual realizations are obtained.

Simulations were then performed of near-critical Rayleigh–Bénard flow. These computations were based on an extended version of the SPM constructed in [13]. Attention was focused on the case of uncertain hot-wall temperature, selected so that both stable and unstable behavior are likely to occur. Similar to earlier experiences with the model dynamical system, the simulations indicate that the WHa scheme effectively captures the transition, as well as the statistics of the stochastic process. In contrast, the WLe expansion suffered from several limitations, including poor prediction of transition and of the state of the system, especially in the case of stable realizations. The WHa and WLe schemes were also applied in situations involving smooth dependence on the random data, which were selected such that recirculating flow is established for all realizations. In this situation, both schemes performed in a satisfactory fashion with the WLe scheme exhibited a superior rate of convergence.

The present experiences point to a number of interesting extensions of the present approach, including hybrid formulations combining wavelets and spectral expansions, and adaptive wavelet formulations. These extensions, as well as generalizations to multiple stochastic dimensions, are currently being explored.

References

[1] S. Wiener, The homogeneous chaos, Am. J. Math. 60 (1938) 897–936.
[2] R. Cameron, W. Martin, The orthogonal development of nonlinear functionals in series of Fourier-Hermite functionals, Ann. Math. 48 (1947) 385–392.
[3] A. Chorin, Hermite expansions in Monte-Carlo computation, J. Comput. Phys. 8 (1971) 472–482.
[4] F. Maltz, D. Hitzl, Variance reduction in Monte Carlo computations using multi-dimensional Hermite polynomials, J. Comput. Phys. 32 (1979) 345–376.
[5] W. Meecham, D. Jeng, Use of the Wiener–Hermite expansion for nearly normal turbulence, J. Fluid Mech. 32 (1968) 225.
[6] S. Crow, G. Canavan, Relationship between a Wiener–Hermite expansion and an energy cascade, J. Fluid Mech. 41 (1970) 387–403.
[7] A. Chorin, Gaussian fields and random flow, J. Fluid Mech. 63 (1974) 21–32.
[8] R. Ghanem, P. Spanos, Stochastic Finite Elements: A Spectral Approach, Springer, Berlin, 1991.

[9] H. Matthies, C. Brenner, C. Bucher, C. Soares, Uncertainties in probabilistic numerical analysis of structures and solids – stochastic finite-elements, Struct. Safety 19 (3) (1997) 283–336.
[10] R. Ghanem, S. Dham, Stochastic finite element analysis for multiphase flow in heterogeneous porous media, Transport Porous Media 32 (1998) 239–262.
[11] R. Ghanem, Probabilistic characterization of transport in heterogeneous media, Comput. Methods Appl. Mech. Eng. 158 (1998) 199–220.
[12] O. Le Maître, O. Knio, H. Najm, R. Ghanem, A stochastic projection method for fluid flow. I. Basic formulation, J. Comput. Phys. 173 (2001) 481–511.
[13] O. Le Maître, M. Reagan, H. Najm, R. Ghanem, O. Knio, A stochastic projection method for fluid flow. II. Random process, J. Comput. Phys. 181 (2002) 9–44.
[14] O.P. Le Maître, M.T. Reagan, B. Debusschere, H.N. Najm, R.G. Ghanem, O.M. Knio, Natural convection in a closed cavity under stochastic, non-Boussinesq conditions, SIAM J. Sci. Comput. (submitted).
[15] T. Hien, M. Kleiber, Stochastic finite element modelling in linear transient heat transfer, Comput. Methods Appl. Mech. Eng. 144 (1997) 111–124.
[16] O.P. Le Maître, O.M. Knio, B.D. Debusschere, H.N. Najm, R.G. Ghanem, A multigrid solver for two-dimensional stochastic diffusion equations, Comput. Methods Appl. Mech. Eng. 192 (2003) 4723–4744.
[17] B. Phenix, J. Dinaro, M. Tatang, J. Tester, J. Howard, G. McRae, Incorporation of parametric uncertainty into complex kinetic mechanisms: application to hydrogen oxidation in supercritical water, Combust. Flame 112 (1998) 132–146.
[18] B. Debusschere, H. Najm, A. Matta, O. Knio, R. Ghanem, O. Le Maître, Protein labeling reactions in electrochemical microchannel flow: numerical prediction and uncertainty propagation, Phys. Fluids 15 (2003) 2238–2250.
[19] M. Reagan, H. Najm, R. Ghanem, O. Knio, Uncertainty quantification in reacting flow simulations through non-intrusive spectral projection, Combust. Flame 132 (2003) 545–555.
[20] D. Xiu, G. Karniadakis, Modeing uncertainty in steady state diffusion problems via generalized polynomial chaos, Comput. Methods Appl. Mech. Eng. 191 (2002) 4927–4948.
[21] D. Xiu, G. Karniadakis, The Wiener–Askey polynomial chaos for stochastic differential equations, SIAM J. Sci. Comput. 24 (2002) 619–644.
[22] D. Xiu, G. Karniadakis, Modeling uncertainty in flow simulations via generalized polynomial chaos, J. Comput. Phys. 187 (2003) 137–167.
[23] M. Deb, I. Babuska, J. Oden, Solution of stochastic partial differential equations using Galerkin finite element techniques, Comput. Methods Appl. Mech. Eng. 190 (2001) 6359–6372.
[24] I. Daubechies, Tens Lectures on Wavelets, SIAM, Philadelphia, PA, 1992.
[25] R.T. Ogden, Essentials Wavelets for Statistical Applications and Data Analysis, Birkhäuser, Basel, 1997.
[26] G.G. Walter, Wavelets and Other Orthogonal Systems with Applications, CRC Press, Boca Raton, 1994.
[27] D.F. Walnut, An Introduction to Wavelets Analysis, Applied and Numerical Harmonic Analysis, Birkhäuser, Basel, 2002.
[28] O. Knio, R. Ghanem, Polynomial chaos product and moment formulas: a user utility, Technical Report, The Johns Hopkins University, Baltimore, MD, 2001 (unpublished).
[29] G. Batchelor, An Introduction to Fluid Dynamics, Cambridge University Press, Cambridge, 1985.
[30] P. Le Quéré, Accurate solution to the square thermally driven cavity at high Rayleigh Number, Comput. Fluids 20 (1) (1991) 29–41.
[31] P. Drazin, W. Reid, Hydrodynamic Stability, Cambridge University Press, Cambridge, 1982.
[32] B. Gebhart, Y. Jaluria, R. Mahajan, B. Sammakia, Buoyancy-induced Flows and Transport, Hemisphere, Washington, DC, 1988.